TAMPEREEN TEKNILLINEN YLIOPISTO
TAMPERE UNIVERSITY OF TECHNOLOGY

PETTERI SIPPOLA

VALIDATING A TRIBOELECTRIC CHARGING AND ELECTROSTATICS MODEL FOR GAS-PARTICLE FLOWS

Master of Science thesis

Examiner: Prof. Pentti Saarenrinne
Examiner and topic approved by the
Faculty Council of the Faculty of
Natural Sciences
on 9st November 2016

ABSTRACT

PETTERI SIPPOLA: Validating a triboelectric charging and electrostatics model for gas-particle flows
Tampere University of Technology
Master of Science thesis, 71 pages, 5 Appendix pages
May 2018
Master's Degree Programme in Environmental and Energy Engineering
Major: Energy Efficiency
Examiner: Prof. Pentti Saarenrinne
Keywords: Gas-particle flow, fluidized bed, triboelectric charging

In fluidized beds and pneumatic conveyors triboelectric charging is generally an undesirable phenomenon, as it causes agglomeration of charged particles on the walls. At worst, agglomeration of the particles and other side-effects of triboelectric charging can reduce the performance of a fluidized bed or a conveyor significantly.

In the thesis, a triboelectric charging model built onto a CFD-DEM (Computational Fluid Dynamics-Discrete Element Method) model is utilized for simulating a small fluidized bed of monodisperse particles. In the model, charge transfer is governed by the effective work function difference between the particles and the wall.

The simulation results are compared to experimental results measured in relative humidities ranging from 0 % to 60 %. It is found that the simulations capture qualitatively the most appreciable side-effect of triboelectric charging, as a layer of strongly charged particles is adhered to the wall. However, this phenomenon is not as pronounced as in the experiments, where multiple layers of particles agglomerate on the wall.

This discrepancy between the simulations and the experiments reflects to other aspects as well: for example the pressure drop over a simulated bed shows almost no change during the fluidization, while in the experiments a significant decrease in pressure drop is observed due to particle agglomeration. For more realistic results, the agglomeration of the particles should be better captured by the computational model.

TIIVISTELMÄ

PETTERI SIPPOLA: Kitkavarautumismallin validointi kaasu-partikkelivirtauksessa
Tampereen teknillinen yliopisto
Diplomityö, 71 sivua, 5 liitesivua
Toukokuu 2017
Ympäristö- ja energiatekniikan koulutusohjelma
Pääaine: Energiatehokkuus
Tarkastajat: Prof. Pentti Saarenrinne
Avainsanat: Kaasu-partikkelivirtaus, leijupeti, kitkavarautuminen

Kitkavarautuminen leijupedeissä ja pneumaattisissa kuljettimissa aiheuttaa muun muassa partikkeleiden tarttumista ja kasaantumista seinämille. Tämä yhdessä muiden lieveilmiöiden kanssa voi pahimmassa tapauksessa huonontaa leijupedin tai kuljettimen toimintaa merkittävästi.

Tässä työssä simuloidaan pienikokoista leijupetiä käyttäen CFD-DEM (engl. Computational Fluid Dynamics-Discrete Element Method) mallin oheen rakennettua vaurautumismallia. Mallissa varauksen siirtymistä hallitsee niin kutsuttu efektiivinen työfunktioero leijutettujen partikkeleiden ja seinämän välillä.

Simulaatiotuloksia verrataan kokeellisesta leijupedistä saaatuihin tuloksiin, jotka on mitattu 0-60 %:n suhteellisessa kosteudessa. Samaan tapaan kuin kokeellisessa leijupedissä, simuloidussa pedissä seinämälle kertyy voimakkaasti varautuneista partikkeleista muodostuva kerros. Ilmiön voimakkuus ei kuitenkaa vastaa kokeellisesta pedistä tehtyjä havaintoja; käytännössä seinämälle kasautuu useita kerroksia partikkeleita.

Tämä ero simulaatioiden ja kokeellisten tulosten välillä heijastuu myös muihin vertailtaviin osa-alueisiin: esimerkiksi painehäviö simuloidussa pedissä ei juuri muutu leijutuksen aikana, vaikka kokeellisessa pedissä painehäviö pienenee merkittävästi partikkeleiden kasautumisen seurauksena. Realistisempien tulosten saavuttamiseksi laskentamallin täytyisi kuvata paremmin partikkeleiden kasautuminen seinämille.

PREFACE

The triboelectric charging model used in this work has been originally implemented on OpenFOAM®by Jari Kolehmainen and Ali Ozel in Princeton University, and is modified and reviewed by the author to enable simulating a fluidized bed with insulating walls.

My sincere thanks to Pentti and Jari for patiently guiding me during the course of this work. Many thanks to people in Princeton for considering the the modifications and additions made to the computational model, as well as to the people downstairs for their invaluable aid when assembling the experimental setup.

Tampere, 24.5.2017

Petteri Sippola

TABLE OF CONTENTS

LIST OF FIGURES

LIST OF TABLES

LIST OF ABBREVIATIONS AND SYMBOLS

Abbreviations

CFD Computational fluid dynamics

COR Coefficient of restitution

DEM Discrete element method

DPM Discrete particle method

FVM Finite volume method

Symbols

α volume fraction of fluid

$\boldsymbol{\delta}_n$ tangential displacement

$\boldsymbol{\delta}_n$ tangential displacement

$\boldsymbol{\tau}$ viscous stress tensor

$\Delta\varphi$ Effective work function difference

δ_n normal displacement

η_n damping coefficient in normal direction

η_t damping coefficient in tangential direction

λ bulk viscosity

$\mathrm{Re}_{\mathrm{rel}}$ Relative Reynolds number of a particle

$\mathbf{F}$ force acting on a particle

$\mathbf{f}$ force per unit volume acting on a fluid

$\mathbf{g}$ gravitational acceleration

$\mathbf{n}$ normal vector

$\mathbf{u}$ velocity of fluid

$\mathbf{v}$	velocity of a particle
μ	dynamic viscosity
ν	Poisson's ratio
ϕ	electric potential
ρ	mass density
ρ_q	charge density
σ	surface charge density
ε	electric permittivity
φ	effective work function
A	contact area
A	cross-sectional area of the fluidized bed
D	diameter of a particle
E	Electric field
e	elementary charge
f_{drag}	drag factor
$f_{\text{drag,0}}$	drag factor of an isolated particle
G	shear modulus
k_n	stiffness coefficient in normal direction
k_t	stiffness coefficient in tangential direction
m	mass
p	pressure
Q	Total charge of particles
q	Charge of a particle
Q_∞	Saturation charge accounting for all the particles in the bed

q_∞	saturation charge of a particle
q_{eq}	equilibrium charge
r	radius of a particle
S	surface area
T	torque acting on a particle
t	time
V	volume
x	Position vector
Y	elastic modulus (Young's modulus)
z	gap between surfaces
z_c	critical charge transfer distance (over which a charge carrier has a reasonably probability to transfer)

1. INTRODUCTION

When two different materials are brought into contact, a net charge transfer may occur when the surfaces are separated again. This phenomenon is known as "contact electrification". If friction is involved, the phenomenon is known as "triboelectric charging" or simply "tribocharging" [1]. In this work, charge transfer between contacting surfaces is referred as triboelectric charging even if no friction is involved.

Triboelectric charging is a commonly known phenomenon, but the exact nature of the charge transferred in a contact of two insulating materials is rather poorly understood. Still, applications utilizing triboelectric charging has been developed for example in electrostatic powder coating, waste separation and even in energy production through triboelectric nanogenerators [2]. [3–5].

On the other hand, in fluidized beds and pneumatic conveyors triboelectricity tends to be problematic: electrostatic forces cause triboelectrically charged particles to agglomerate on the walls, lowering the performance of the device. Despite agglomeration, electrostatic forces influence the bubble size and shape and particle mixing rate in gas-solid fluidized beds. [1, 6–8].

The aim of this study is to investigate if a relatively simple triboelectric charging model based on the concept of the *effective work function difference* can correctly predict the behaviour of a small fluidized bed of monodisperse polyethylene particles. The computational model is not restricted to fluidized beds only, but could be used to simulate any type of gas-particle flow.

It is commonly known that electrostatic effects diminish in humid conditions. On the other hand, humid air probably serves as a source of charge through introducing ions on the surfaces [3]. The experiments in this work are conducted in different relative humidities to study the effect of humidity to the tribolectric charging in the bed.

The rest of this text is divided to the theoretical background, the experimental setup, the simulation setup and finally the results and discussion. The theoretical background is divided into two chapters: a chapter describing the theory of fluid dynamics and particles and a chapter discussing the effects of electrostatics and triboelectric charging.

2. FLUID DYNAMICS AND PARTICLES

In this chapter, the constitutive equations of fluid dynamics are discussed before proceeding into the interaction of fluid and particles. To keep it short, the discretization procedures required for actual implementation of the model are only briefly discussed. The interaction between fluid and particles is considered last.

2.1 Fluid dynamics

Fluid dynamics is a subdiscipline of fluid mechanics, namely the study of fluids in motion [9]. Fluid mechanics in turn can be classified as a branch of continuum mechanics, which means that the fluid is modeled as a continuous mass rather than as individual particles [10]. In this chapter, the principles of fluid dynamics are studied through examining the most basic equations related to fluid motion. The equations are considered in the context of the finite volume method (FVM), which is the preferred method in computational fluid dynamics (CFD) [11].

2.1.1 Constitutive equations

In general, the equations describing a fluid flow are a collection of conservation equations justified by physical principles. The most important equations dealing with fluid flow are the conservation of mass, momentum and energy [11]. In this section, only the conservation of mass and the momentum are considered, as they are the most relevant ones in this work.

Conservation of mass

Consider an arbitrary, stationary control volume containing any fluid. In normal conditions, no mass is being created nor destroyed in the control volume, hence the

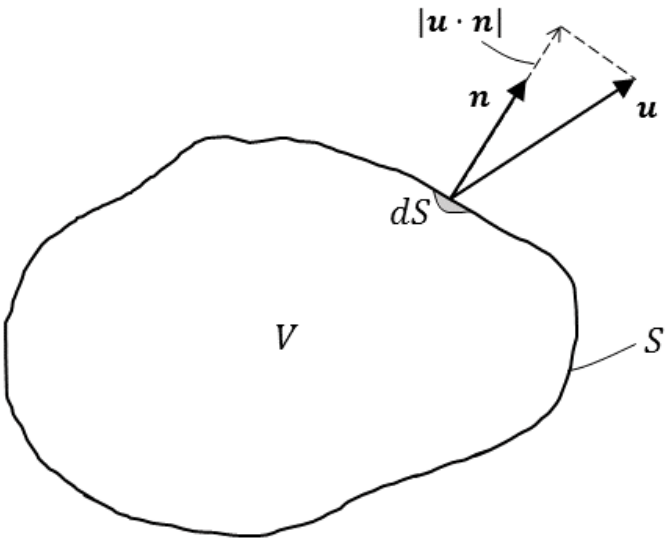

Figure 2.1 *A stationary control volume V enclosed by surface S.*

mass in the control volume can only change due to a flow through the boundary. Mathematically this can be expressed as

$$\frac{d}{dt}\int_V \rho\, dV = -\int_S \rho(\mathbf{u}\cdot\mathbf{n})\, dS, \tag{2.1}$$

where ρ and $\mathbf{u}$ are the density and the velocity of the fluid at a given point and $\mathbf{n}$ is the unit normal pointing outwards at the boundary. Both the density and the velocity are functions of position and time, although it is not explicitly expressed in the equation. [11]

The left hand side of Equation 2.1 represents the instantaneous change of mass in the control volume. On the right hand side, the dot product $(\mathbf{u}\cdot\mathbf{n})$ can be recognized as the velocity component directed outwards from the control volume. This is illustrated in Figure 2.1. Multiplying the outwards pointing velocity with mass density at given point, one obtains the mass outflow per surface area at that point. Integrating the flow rate per area over the control surface S results in the net mass flow rate out of the control volume. [11]

As the control volume is stationary, the volume over which the density is integrated is constant. In such a situation, the Reynolds transport theorem allows one [12] to

modify the right side of Equation 2.1 so that

$$\frac{d}{dt}\int_V \rho\, dV = \int_V \frac{\partial \rho}{\partial t}\, dV. \tag{2.2}$$

This is self-evident when Equation 2.2 is verbalized: the change of the total mass in a static control volume equals the total change of mass inside the volume.

Substituting Equation 2.2 into Equation 2.1 and utilising the divergence theorem, the continuity equation becomes

$$\int_V \left[\frac{\partial \rho}{\partial t} + \nabla \cdot (\rho \mathbf{u})\right] dV = 0. \tag{2.3}$$

For this to be true to for any arbitrary sized control volume, the integrand must be zero. This leads to the differential form of the continuity equation:

$$\frac{\partial \rho}{\partial t} + \nabla \cdot (\rho \mathbf{u}) = 0. \tag{2.4}$$

For incompressible fluids the density is constant, so the continuity equation simplifies to

$$\nabla \cdot \mathbf{v} = 0. \tag{2.5}$$

One consequence of Equation 2.5 is that if at any point the speed of the flow is decreasing in any direction, the speed must increase in some other direction. Otherwise, mass would accumulate on the point, increasing the density. [11]

Conservation of linear momentum

The change of linear momentum inside a control volume V originates either from momentum exchange over the boundary or from external forces affecting on the volume. Combining these two effects and utilising the Reynolds transport theorem, one obtains

$$\frac{d}{dt}\int_V \rho \mathbf{u}\, dV = \int_V \mathbf{f}\, dV - \int_S \rho \mathbf{u}(\mathbf{v} \cdot \mathbf{n})\, dS, \tag{2.6}$$

where $\mathbf{f}$ is force per unit volume affecting on the control volume. [11]

The product $(\rho \mathbf{u})$ in Equation 2.6 can be recognized as the momentum per unit volume, hence the integral on the left hand side represents the instantaneous change

of the linear momentum inside the control volume. On the right hand side, the surface integral over boundary S gives the momentum flow rate over the boundary. All the integrals result in a vector; the linear momentum is conserved separately in every coordinate direction.

The surface integral in Equation 2.6 can be reformulated by introducing a dyadic tensor product $\mathbf{uu}$ of the velocity vector, which can be represented as a matrix equation

$$\mathbf{uu} = \begin{bmatrix} uu & uv & uw \\ vu & vv & vw \\ wu & wv & ww \end{bmatrix}, \tag{2.7}$$

where u, v and w are the x-, y- and z-components of the velocity vector $\mathbf{u}$, respectively [11]. Taking the dot product with the surface normal vector $\mathbf{n}$ results in

$$(\mathbf{uu}) \cdot \mathbf{n} = \begin{bmatrix} uu & uv & uw \\ vu & vv & vw \\ wu & wv & ww \end{bmatrix} \begin{bmatrix} n_x \\ n_y \\ n_z \end{bmatrix} = \begin{bmatrix} uun_x + uvn_y + uwn_z \\ vun_x + vvn_y + vwn_z \\ wun_x + wvn_y + wwn_z \end{bmatrix} = \mathbf{u}(\mathbf{u} \cdot \mathbf{n}), \tag{2.8}$$

which substituted into Equation 2.6 and rearranging results in

$$\frac{d}{dt} \int_V \rho \mathbf{u} \, dV + \int_S (\rho \mathbf{uu}) \cdot \mathbf{n} \, dS - \int_V \mathbf{f} \, dV = 0. \tag{2.9}$$

Utilising the divergence theorem again one obtains the differential form of the linear momentum equation [11]

$$\frac{\partial(\rho \mathbf{u})}{\partial t} + \nabla \cdot (\rho \mathbf{uu}) - \mathbf{f} = 0. \tag{2.10}$$

The differential form of the momentum equation is more compact than the integral form, although perhaps not as intuitively clear due to the involvement of the dyadic tensor product. However, the divergence term $\nabla \cdot (\rho \mathbf{uu})$ can be understood as the net momentum flow rate out of an infinitesimal control volume, which emphasizes the equivalence of equations 2.9 and 2.10.

2.1.2 Forces affecting on a fluid

The forces affecting on a fluid can be divided into two classes: body forces and surface forces. The body forces are defined as forces affecting on a volume: as an

example of body forces, the force per unit volume due to gravity is

$$\mathbf{f}_g = \rho \mathbf{g}, \tag{2.11}$$

where $\mathbf{g}$ is the gravitational acceleration. [11]

Surface forces are stresses acting on any real or fictitious surface in the fluid. These are classified into normal stresses and shear stresses, depending on the direction of the stress in relation with the surface. [11]

The most prominent of the normal stresses is the thermodynamic pressure, which at any point exerts a similar magnitude of force to any surface, independent of the surface direction [11]. The force per unit area exerted by pressure can be represented as

$$\mathbf{p} = -p\mathbf{n}, \tag{2.12}$$

where $\mathbf{p}$ is the resulting pressure, p is the thermodynamic pressure (scalar) and $\mathbf{n}$ is the unit normal vector pointing outwards from the control surface.

Viscous stresses are more complicated to evaluate than the pressure, as their magnitude and direction depends on the direction of the surface they affect on. Anyhow, viscous stress can be expressed conveniently in terms of stress tensor $\boldsymbol{\tau}$, which describes the viscous stresses affecting on surfaces perpendicular to each coordinate axle. The viscous stress acting on an arbitrary surface are obtained as the dot product of the surface normal and the stress tensor. [11]

Assuming that the viscous stresses and the pressure are the only surface forces involved and the gravity is the only body force present, the momentum equation (Equation 2.10) becomes

$$\frac{\partial(\rho \mathbf{u})}{\partial t} + \nabla \cdot (\rho \mathbf{u}\mathbf{u}) = -\nabla p + \nabla \cdot \boldsymbol{\tau} + \rho \mathbf{g}, \tag{2.13}$$

where $-\nabla p$ is the force due to the pressure gradient and $\nabla \cdot \boldsymbol{\tau}$ is the contribution of viscous stresses.

Viscous stresses

In order to solve the fluid flow from Equation 2.13, the viscous stresses have to be linked to the state of the flow. For Newtonian fluids the viscous stress tensor is [11]

$$\boldsymbol{\tau} = \mu \begin{bmatrix} 2\frac{\partial u}{\partial x} + \frac{\lambda}{\mu}\nabla \cdot \mathbf{v} & \frac{\partial v}{\partial x} + \frac{\partial u}{\partial y} & \frac{\partial w}{\partial x} + \frac{\partial u}{\partial z} \\ \frac{\partial u}{\partial y} + \frac{\partial v}{\partial x} & 2\frac{\partial v}{\partial y} + \frac{\lambda}{\mu}\nabla \cdot \mathbf{v} & \frac{\partial w}{\partial y} + \frac{\partial v}{\partial z} \\ \frac{\partial u}{\partial z} + \frac{\partial w}{\partial x} & \frac{\partial v}{\partial z} + \frac{\partial w}{\partial y} & 2\frac{\partial w}{\partial z} + \frac{\lambda}{\mu}\nabla \cdot \mathbf{v} \end{bmatrix}, \tag{2.14}$$

For incompressible fluids, a contribution of the bulk viscosity λ is zero, as $\nabla \cdot \mathbf{v} = 0$. If the dynamic viscosity μ is constant and the fluid is incompressible, Equation 2.13 simplifies to

$$\frac{\partial(\rho \mathbf{u})}{\partial t} + \nabla \cdot (\rho \mathbf{u}\mathbf{u}) = -\nabla p + \mu \nabla^2 \mathbf{u} + \rho \mathbf{g}. \tag{2.15}$$

Along with appropriate boundary conditions, this kind of equation along with the continuity equation could be utilised to describe a fluid flow by means of CFD, if only one phase was present.

2.2 Fluids containing a dispersed phase

In this work we are dealing with a gas-particle flow, in which solid particles are dispersed in a continuous fluid (gas) phase. Computationally, the presence of the particles is accounted by the forces exerted on the fluid and by the volume fraction of particles in each computational cell.

In this work, the volume fraction of the fluid is denoted by α, so the respective volume fraction of the particle phase is $1 - \alpha$. The *bulk density* of the fluid can then be expressed as

$$\bar{\rho} = \alpha \rho, \tag{2.16}$$

where ρ is the material density of the fluid [13]. Integrating the bulk density over a control volume V results in

$$\int_V \bar{\rho}\, dV = \int_V \alpha \rho\, dV = m_f, \tag{2.17}$$

where m_f denotes the mass of the fluid inside the control volume.

The dispersed phase can be taken into account in the continuity equation just by substituting the material density with the bulk density, which results in

$$\frac{d}{dt}\int_V \alpha\rho \, dV = -\int_S \alpha\rho(\mathbf{u}_f \cdot \mathbf{n}) \, dS. \tag{2.18}$$

Similarly, the momentum equation becomes

$$\frac{d}{dt}\int_V \alpha\rho\mathbf{u} \, dV = \int_V \alpha\mathbf{f} \, dV - \int_S \alpha\rho\mathbf{u}(\mathbf{v} \cdot \mathbf{n}) \, dS. \tag{2.19}$$

In differential form, these equations can be expressed as

$$\frac{\partial\alpha\rho}{\partial t} + \nabla \cdot (\alpha\rho\mathbf{u}) = 0. \tag{2.20}$$

and

$$\rho\frac{\partial(\alpha\mathbf{u})}{\partial t} + \rho\nabla \cdot (\alpha\mathbf{u}\mathbf{u}) - \mu\nabla^2\alpha\mathbf{v} + \frac{\nabla p}{-}\alpha\rho\mathbf{g} = 0, \tag{2.21}$$

if the viscosity is taken to be constant and the fluid is incompressible. The differential equations are clearly more convenient than the integral ones, but the integral form is more close to the actual computational implementation as seen in the next section.

2.3 The finite volume method

The finite volume method bases on dividing the region of interest into a contiguous mesh of finite control volumes (cells). The fluid is regarded as a continuum, so the size of the cells has to be several orders of magnitude greater than molecular scales. In FVM, the change of the properties (for instance the mass, the momentum and the kinetic energy) of each cell over time are evaluated from the property fluxes over the cell faces. [11, 13]

The constitutive equations can be readily discretized by treating each cell as a closed volume and applying the respective equations to the cell. For example, the continuity equation Equation 2.1 for a certain cell becomes

$$\frac{d}{dt}\rho_c = -\frac{1}{V_c}\sum_f \mathbf{S}_f \cdot (\rho\mathbf{u})_f, \tag{2.22}$$

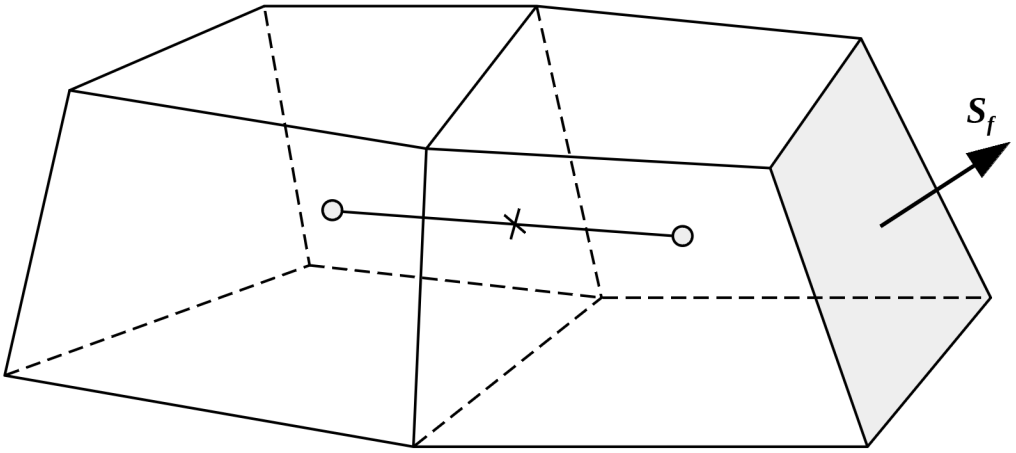

Figure 2.2 *Two hexahedral cells with a common face. The face-area vector* $\mathbf{S}_f$ *is marked for the rightmost face. The grey dots mark the centroids of the two faces and the black cross marks the intersection of the internal face and the line joining the cell centroids.*

where ρ_c and V_c are the mass density and the volume of cell, respectively. The summation on the right hand side runs over all the faces f of the cell. The mass flow rate over each face is $\mathbf{S}_f \cdot (\rho \mathbf{u})_f$, where $\mathbf{S}_f = S_f \mathbf{n}_f$ is an face area vector pointing outwards from the cell. [14]

In a similar fashion, the discretized momentum equation for an incompressible fluid with a constant viscosity can be expressed as

$$\frac{d}{dt}(\rho \mathbf{u})_c = \rho_c g - \frac{1}{V_c} \sum_f \mathbf{S}_f \cdot \left[(\rho \mathbf{u})_f \mathbf{u}_f - \mu (\nabla \mathbf{u})_f + p_f \right], \tag{2.23}$$

where $(\rho \mathbf{u})_c$ is the momentum per volume in the cell, $\mathbf{f}_c$ is the total body force per volume affecting on the cell. The sum on the right hand side accounts for the contribution of the momentum flux, the viscous stresses and the pressure over the cell faces.

The accuracy of the solution depends on how well the fluxes over the faces are approximated. The usual approach in FVM is to approximate the flux over a face by interpolating the quantities of the adjacent cells to the geometric centroids of the face: for example, if the mass densities of the cells in Figure 2.2 are ρ_A and ρ_B, the density at the common face could be obtained by interpolating ρ_A and ρ_B according to the distance of the cell centers to the face. This renders second-order accuracy

for the values of both the cells and the faces. [11]

Equation 2.23 is formulated according to the the discretization methods of OpenFOAM [14]; similar equations could be obtained when taking into account the volume fraction of the fluid. The actual solution algorithms for solving the of the continuity and momentum equations while accounting for the dispersed phase in OpenFOAM are pretty complicated, and are limited out of the scope this text.

2.4 Equations of particle motion

The motion of a particle is affected by the force exerted by the fluid and contact forces with the other particles and the wall. Equations describing translational and rotational motion of a particle are

$$m_i \frac{d\mathbf{v_i}}{dt} = \sum_j (\mathbf{F}^n_{c,ij} + \mathbf{F}^t_{c,ij}) + \sum_w (\mathbf{F}^n_{c,iw} + \mathbf{F}^t_{c,iw}) + \mathbf{F}_{e,i} + \mathbf{F}_{g\to p,i} + m_i\mathbf{g} \tag{2.24}$$

$$I_i \frac{d\omega_\mathbf{i}}{dt} = \sum_j \mathbf{T}_{t,ij} + \sum_w \mathbf{T}_{t,iw}, \tag{2.25}$$

where $\mathbf{v_i}$ and $\omega_\mathbf{i}$ are the translational and rotational velocities of particle i having mass m_i and a moment of inertia I_i. The contact forces acting on the particle are decomposed into normal (subscript n) and tangential forces (subscript t) arising from contacts with other particles (subscript j) and contacts with walls (subscript w). [13], [15]

The other forces acting on the particle are the electrostatic force $\mathbf{F}_{e,i}$, the force due to the surrounding gas ($\mathbf{F}_{g\to p,i}$) and the gravitational force $m_i\mathbf{g}$, where $\mathbf{g}$ is the gravitational acceleration. The force exerted by the gas to the particle can be divided into the steady-state drag force, the unsteady forces, the undisturbed pressure force, the undisturbed viscous stress force and the lift forces due to particle rotation, respectively:

$$\mathbf{F}_{g\to p} = \mathbf{F}_d + \mathbf{F}_p + \mathbf{F}_\tau + \mathbf{F}_{\text{unsteady}} + \mathbf{F}_{\text{lift}}. \tag{2.26}$$

These forces are discussed in detail in the next section. To put it short, only the steady-state drag term $\mathbf{F}_d$ is significant in a gas-particle flow. [13]

The torque acting on a particle is decomposed to the torque $\mathbf{T}_{t,ij}$ caused by another

particles and the torque $\mathbf{T}_{t,ij}$ caused by the wall contacts. According to basic mechanics, the torque acting on particle i can be calculated from the contact forces as

$$\mathbf{T}_i = \sum_{c,i} \mathbf{r}_{c,i} \times \mathbf{F}_{c,i}, \tag{2.27}$$

where the sum is over all the contact forces $\mathbf{F}_c$ acting on particle i and $\mathbf{r}_c$ is the displacement between the particle center and the respective contact point. In the next sections, the models for calculating the components of the momentum equation are explained.

2.5 Particle-particle interaction

There exists two primary models to describe collisions between spherical particles: the hard-sphere model and the soft-sphere model. The hard sphere model is based on integrated equations of motion and gives the relationship between the velocities before and after the collision, whereas the soft-sphere model describes the motion of the particles during the collision [13]

Despite of the greater computational cost, the soft-sphere model is the viable option in a dense particle flow, as it is capable of handling multiple simultaneous collisions [13]. As discussed later, the soft-sphere model also provides a straightforward way to compute the charge transfer when triboelectric charging is involved.

The soft-sphere model was originally proposed by Cundall and Strack [16]. The equations presented in this chapter match well with the numerical implementation of standard `OpenFOAM` and are formulated following Crowe *et al.* [13]. In addition to the the original implementation of OpenFOAM, the modified version used in this study allow one to calculate the damping coefficient with respect to the coefficient of restitution (Equation 2.31).

In the soft-sphere model the total force between colliding particles is represented in terms of *stiffness*, *damping coefficient* and *friction coefficient*. Stiffness attributes to a repulsive force due to the displacement of the particles, whereas the damping force is proportional to the relative velocity of the particles. The friction force in turn is dependent on the relative tangential velocity of the surfaces in contact. [13]

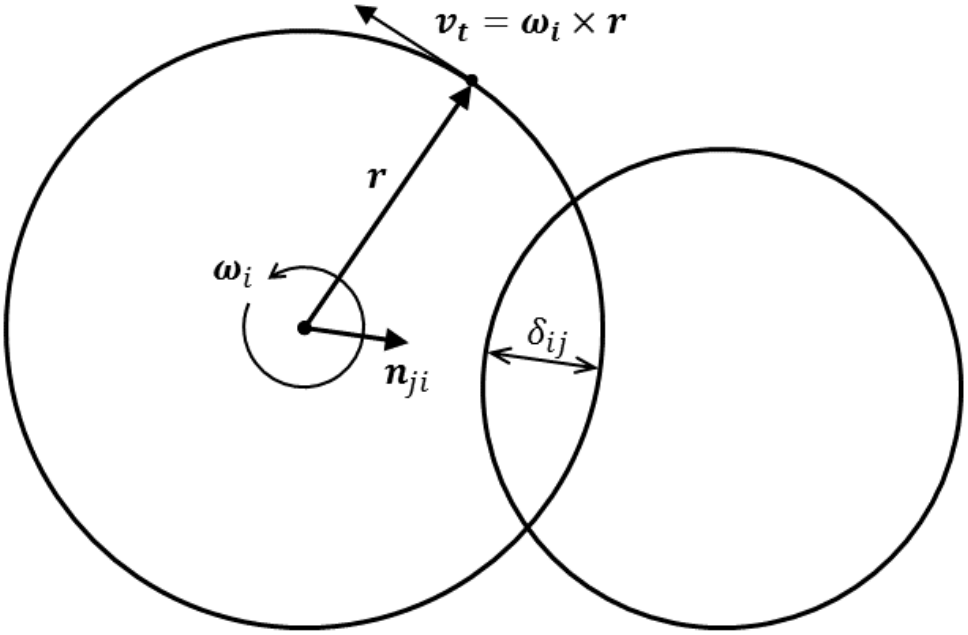

Figure 2.3 *Two spherical particles in contact.* $\mathbf{n}_{ji} = -\mathbf{n}_{ij}$ *is an unit vector pointing from particle* i *to particle* j

The normal contact force on particle i due to particle j is

$$\mathbf{F}_{ij}^n = k_n \delta_n^{3/2} \mathbf{n}_{ij} - \eta_n \mathbf{v}_{ij}^n, \tag{2.28}$$

where k_n and η_n are the stiffness and the damping coefficient in the normal direction, respectively and $\mathbf{n}_{ij}$ is an unit vector pointing from the center of particle i to the center of particle j. The normal displacement δ_n is defined as the normal intersection distance of the particles if they would not deform as (see Figure 2.3). The normal component of the relative velocity between the particles is $\mathbf{v}_{ij}^n = ((\mathbf{v}_i - \mathbf{v}_j) \cdot \mathbf{n}_{ij})\mathbf{n}_{ij}$. [13]

According to the Hertzian contact model the stiffness coefficient k_n is

$$k_n = \frac{4}{3} Y^* \sqrt{r^*}, \tag{2.29}$$

where Y^* and r^* are is the equivalent elastic modulus (Young's modulus) and the equivalent radius of the colliding particles (See definition of equivalent properties in Equation 2.36. Tsuji et al. found heuristically that if the damping coefficient is

given by

$$\eta_n = \alpha_{\mathrm{COR}}(m^* k_n)^{1/2}\delta_n^{1/4}, \tag{2.30}$$

where α_{COR} is a function of the coefficient of restitution (COR), the coefficient of restitution becomes independent of the combination of the stiffness factor, the damping factor and the equivalent mass m^*. This is allows the damping coefficient to be calculated from the empirically measurable value of the coefficient of restitution. [17].

Tsuji et al. only gave a numerical result for α_ϵ. It has been since shown that

$$\alpha = -\ln(\mathrm{COR})\sqrt{\frac{5}{\ln(\mathrm{COR})^2 + \pi^2}} \tag{2.31}$$

is the respective analytical result [18].

The tangential contact force for non-sliding contact is [17]

$$\mathbf{F}_{ij}^t = -k_t\boldsymbol{\delta}_t - \eta_t\mathbf{v}_{ij}^t, \tag{2.32}$$

where k_t and η_t are the tangential stiffness and damping coefficients, $\boldsymbol{\delta}_t$ is tangential displacement and $\mathbf{v}_{ij}^t$ is the relative velocity of the particle surfaces at the contact point (slip velocity).

As long as the particle surfaces do not slip, the original contact points of the particles stay in touch. This leads to tangential deformation on the particle surfaces, which is described by the tangential displacement. In `OpenFOAM`, tangential displacement is obtained by numerically integrating the slip velocity, which requires tracking all ongoing collisions and storing the displacement corresponding to each collision. If the tangential force exceeds the limit given by sliding friction, the surfaces slide and the tangential displacement of the particular contact is set to zero.

The particle surfaces slip if the tangential force given by Equation 2.32 exceeds $\mu_s|\mathbf{f}_{ij}^n|$, where μ_s is the sliding friction coefficient. In that situation the tangential force is evaluated as

$$\mathbf{F}_{ij}^t = -\mu_s|\mathbf{F}_{ij}^n|\frac{\mathbf{v}_{ij}^t}{|\mathbf{v}_{ij}^t|} \tag{2.33}$$

instead of using Equation 2.32 [17]. This is just the familiar Coulomb friction opposing the slip velocity.

The stiffness coefficient is obtained by using the equivalent shear modulus G^*, the equivalent radius and the normal displacement as

$$k_t = 8G^*\sqrt{r^*\delta_n}. \tag{2.34}$$

The slip velocity is obtained from basic mechanics as

$$\mathbf{v}_{ij}^t = \mathbf{v}_{ij} - \mathbf{v}_{ij}^n + (r_i\omega_i + r_j\omega_j) \times \mathbf{n}_{ij}, \tag{2.35}$$

where r and ω denote the radius and the angular velocity of each particle, respectively. Without further justification Tsuji et al. [17] state that the damping coefficient in the tangential direction approximately equals the coefficient in normal direction, so it is assumed that $\eta_n = \eta_t$. This is also adopted in the standard implementation of OpenFOAM.

The equivalent properties denoted by superscript $*$ are defined as:

$$\begin{aligned} Y^* &\equiv \left(\frac{1-\nu_i^2}{Y_i} + \frac{1-\nu_j^2}{Y_j}\right)^{-1} \\ G^* &\equiv \left(\frac{1-\nu_i}{G_i} + \frac{1-\nu_j}{G_j}\right)^{-1} \\ m^* &\equiv \left(\frac{1}{m_i} + \frac{1}{m_j}\right)^{-1} \\ r^* &\equiv \left(\frac{1}{r_i} + \frac{1}{r_j}\right)^{-1} \end{aligned} \tag{2.36}$$

where the subscripts i and j denote the properties of each particle. In the definitions of G^* and Y^*, ν is Poisson's ratio. For isotropic materials, the shear modulus is connected to the Young modulus by

$$G = Y/2(1+\nu). \tag{2.37}$$

The equations described in this chapter can be used as well for a particle-wall contacts by substituting appropriate equivalent properties. As the mass and the curvature radius of a planar wall are much greater than the mass and radius of a particle, one obtains $m^* = m$ and $r^* = r$ for describing a wall contact of a particle with mass m and radius r. [13]

2.5.1 Particle stiffness and time step in simulations

Tracking colliding particles in DEM-simulations generally demands a time step shorter than about one 10th of the typical duration of a collision [13]. In standard libraries of OpenFOAM, the maximum time step for evaluating particle collisions is calculated as

$$\Delta t_{\max} = \left(\frac{5}{4}\right)^{2/5} \pi^{7/5} r_{\min} \left(Y^* \sqrt{2u_{\max}}\right)^{2/5} (n_{\text{coll}})^{-1}, \tag{2.38}$$

where Y^* is the equivalent Young modulus (different for wall-particle and particle-particle collision), $r_{\min}$ is the minimum particle size, $u_{\max}$ is the maximum particle velocity and $n_{\text{coll}} > 1$ is an user-defined resolution term for the collisions. In the simulations of this study, $n_{\text{coll}} = 10$.

It is clear that in order to allow a greater time step, the Young modulus is the only viable parameter to be altered. Lowering the Young modulus makes the particles appear softer, increases collision times and intersection distances [19]. This also affects the contact area and triboelectric charging, which is further discussed in Section 3.3.

2.6 Particle-fluid interaction

The forces acting on a particle due to the surrounding fluid can be classified in three classes: The forces caused by an undistributed flow, the steady-state forces and unsteady forces [13]. These forces are addressed first before considering the total pressure drop over a fluidized bed caused by the drag force on particles.

2.6.1 Undisturbed flow forces

The undisturbed flow forces are defined as forces that would affect on a particle if the contribution of the particle itself on the flow is neglected. These forces contribute for the velocity and pressure disturbations in the surrounding fluid [13]. The disturbations in the surrounding fluid are of course affected by the surrounding walls, other particles and even the particle itself, which renders the term “undisturbed flow” a bit misleading.

The total force due to the surrounding fluid can be calculated as an integral of the local forces over the particle surface S_p. If the only significant forces present are the pressure and the viscous stresses, the resulting force $\mathbf{F}_{ud}$ would be

$$\mathbf{F}_{g\to p} = \int_{S_p} (\mathbf{n}\cdot\boldsymbol{\tau} - p\mathbf{n})dS_p \tag{2.39}$$

where $\boldsymbol{\tau}$ and p are the shear stress tensor and the pressure in the fluid, respectively, and $\mathbf{n}$ is the unit normal of the surface (pointing outwards).

If the particle is small, Equation 2.39 can be approximated as

$$\mathbf{F}_{g\to p} = V_p(\nabla\cdot\boldsymbol{\tau} - \nabla p), \tag{2.40}$$

where V_p is the volume of the particle. The contributions of the pressure and the viscous stresses are $\mathbf{F}_p = -V_p\nabla p$ and $\mathbf{F}_\tau = V_p\nabla\cdot\boldsymbol{\tau}$, respectively. In practice $\nabla\cdot\boldsymbol{\tau}$ and ∇p would evaluated from the pressure and velocity fields of the fluid at the position of the particle (neglecting the presence of the particle).

When only hydrostatic pressure present, the force due to the pressure equals the weight of the fluid displaced by the particle: $\nabla p = \rho\mathbf{g}$. Substituting $\mathbf{F}_p = -\rho\mathbf{g}V_p$ into Equation 2.24 and combining with the gravity term results in

$$m\mathbf{g} + \mathbf{F}_p = (\rho_p - \rho)V_p\mathbf{g}, \tag{2.41}$$

so the buoyancy could be taken into account by simply subtracting the density of the fluid from the density of the particle when evaluating the equation of motion. In the experiments of the present study the ratio of the densities of the fluid and the particles is

$$\frac{\rho}{\rho_p} \approx 10^{-3}, \tag{2.42}$$

so the buoyancy force can readily be neglected. Also the undistributed viscous stress force is neglected in this study, which is the usual case in gas-particle flows [13].

2.6.2 Steady-state drag

Where the undistributed flow forces neglect the presence of the particle itself, the steady state drag is calculated as a particle was the only one present in the fluid. The steady-state forces apply only for a particle with no relative acceleration between

the particle and the fluid. [13]

The steady-state drag affecting on a particle may be expressed as

$$\mathbf{F}_d = 3\pi\mu D f_{\text{drag}}(\mathbf{u} - \mathbf{v}), \tag{2.43}$$

where D is the particle diameter, f_{drag} is the drag factor, $\mathbf{v}$ is the velocity of the particle and $\mathbf{u}$ is the velocity the surrounding fluid. The drag factor for a spherical particle limits to unity when the relative velocity is small (Stokes flow). In general, the drag factor depends on the Reynolds number

$$\text{Re}_{\text{rel}} = \frac{\rho_f D|\mathbf{v} - \mathbf{u}|}{\mu} \tag{2.44}$$

of the particle. [13]

There exists several correlations for the drag factor for as a function of Reynolds number. One of these is by Schiller and Naumann [20]:

$$f_{\text{drag},0} = (1 + 0.15\text{Re}_{\text{rel}}{}^{0.687}), \tag{2.45}$$

which is valid for an isolated particle up to a relative Reynolds number of 800. The Schiller-Naumann -equation is utilized for calculating the drag coefficient of a single particle in this work, as it is the one used in the drag models already implemented in OpenFOAM.

In addition to the relative velocity, there are numerous other factors affecting on the drag force, such as Faxen force caused by a nonuniform flow field and Magnus force caused by rotation of the particle. However, these are considered negligible in the case of a gas-particle flow [13] and are not considered in this study.

2.6.3 Drag in particle clouds

The drag equation of a single particle can not be directly applied in dense particle clouds, as it does not take into account the contribution of other particles. The local variations of the pressure and shear stresses can be pretty complicated when it comes to a chaotic motion of several particles. However, there exists several experimental correlations considering the effect of the volume fraction on the drag factor.

One of the simplest corrections for the drag factor is by Wen and Yu [21], namely

$$f_{\text{drag}} = \alpha^{-3.7} f_0, \tag{2.46}$$

where α is the fluid volume fraction and f_0 in the drag factor for an isolated particle. Basing on an analysis of existing empirical data, Di Felice [22] have suggested drag factor

$$f_{\text{drag}} = \alpha^{-\beta} f_0, \tag{2.47}$$

where

$$\beta = 3.7 - 0.65 \exp\left[-\frac{(1.5 - \log_{10}(\text{Re}_{\text{rel}})^2}{2}\right]. \tag{2.48}$$

The resulting drag factor does not deviate significantly from the Wen-Yu drag factor. Wen-Yu drag model is included in the standard librariss of OpenFOAM and is utilised in the simulations of this work.

Although the empirical correlations above are originally based on the average volume fraction over entire fluidized bed, in practice the local volume fraction is applied when assigning drag force for a certain particle. This is supposed to be a reasonable estimate of the effect of the local volume fraction on the drag force.

2.6.4 Unsteady forces

The unsteady forces are due to the acceleration and the history of the particle movement. These are known as the *virtual mass effect* and the *Basset force*. The virtual mass effect is due to the acceleration of particle, which causes also acceleration of the displaced fluid. The virtual mass force affecting on a particle is

$$F_{vm} = \frac{\rho V_p}{2}\left(\frac{Du}{Dt} - \frac{dv}{dt}\right), \tag{2.49}$$

where ρ is the density of the fluid, Du/Dt is the total derivative of the fluid velocity at the particle location and dv/dt is the acceleration of the particle [13].

Substituting Equation 2.49 into the equation of motion (Equation 2.24) corresponds to adding a half of the displaced mass to the mass of the particle in the left hand side of the equation. As with the buoyancy force, the fluid density is negligible with respect to the particle density, so the virtual mass effect is neglected in this work.

The Basset term in turn accounts for the history of the particle motion. There exists an analytical result which account for the effect of the preceding motion of an isolated spherical particle [13]. However, this term does not take into account the contribution of other solid objects nearby, which renders the result rather useless in a dense particle cloud. Fortunately also the Basset force is overwhelmed by other forces in a gas-solid flow and not considered in this work.

In the simulations, the history of the particle motion would be partially accounted by the "undisturbed" stress force, as the particle motion affects the velocity field of the fluid. This is one example of how these three types of forces - undisturbed, steady and unsteady forces - have overlapping contributions with each other. The forces are theoretically valid only in ideal situations differing from each other, but are confidently applied together as long as there is no better alternatives.

2.6.5 Pressure drop in a fluidized bed

The pressure drop over a fluidized bed can be approximated by applying the momentum equation over the bed and assuming that at a quasi-stationary state, the pressure drop over the bed counterbalances the total weight of the bed [13, 23]. For a bed with a constant cross sectional area A this would result in

$$\Delta pA = mg, \tag{2.50}$$

where Δp is the pressure drop over the bed and mg is the total weight of the bed.

Equation 2.50 is just a crude approximation, but the dimensionless quantity $\Delta pA/mg$ is convenient to use when considering the pressure loss. Equation 2.50 also relates the mass adhered to the walls of the bed to the decrease in pressure drop.

3. TRIBOELECTRIC CHARGING AND ELECTROSTATICS

In gas-solid fluidized beds, electrostatic forces affect the bubble size and shape, particle mixing rate and agglomeration. If the electrostatic charge on particles is high enough, electrostatic forces cause the particles to adhere to walls. These effects can reduce the performance of commercial fluidized beds, causing plugging, reduced reaction rates and possibly undesirable byproducts. Significant costs may be caused by loss of production if, for example, a polymerization reactor has to be shut down to remove polymer sheets adhered to the wall. In most cases, adhering to the walls is most probably undesirable effect, not to mention pneumatic conveyors. [6, 8, 24].

3.1 Triboelectric charging

The electric charge on particles originates mainly from triboelectric charging, which takes place when particles collide with each other and with surrounding walls [7]. Triboelectric charging is a complicated phenomenon, depending for example on the presence of moisture and oxidising agents in the atmosphere [3, 6]. There is still debate about the nature of the charge transferred in insulator-insulator contacts: some of the authors rely on the electron transfer, whereas others argue that ion transfer is the principal source of charge segregation in insulator-insulator contacts. Some points of the possible charge transfer mechanisms are discussed next.

3.1.1 Effective work function difference

Contact charging between two metals is well understood through the difference of the work functions - the energy required to extract an electron from the surface of the metals. The work function is related to the Fermi level (electrochemical potential of electrons) of the metals; in close proximity, electrons tunnel from metal to metal

until the Fermi levels become balanced. The total charge transfer after separation of the surfaces is limited by the electric potential difference caused by the transferred charge. [25, 26]

Although there exist triboelectric series which approximately predict the charging tendency of insulators in relation to each other, there exists even cyclic transfer cycles between insulators. This indicates that there are most probably more than one charge transfer mechanisms affecting simultaneously. It is not possible to put insulating materials in an unequivocal order basing on their charging tendency. [3]

The term *effective work function* originates from contact electrification occurring in insulator-metal contacts. In early studies of polymer charging, the magnitude of charge transferred was observed to be linearly dependent on the work function of the metal [26, 27]. Accrodingly, the effective work function of an insulator corresponds to the work function of a metal with which no charge exchange transfer would occur.

However, the work function differences related to metals have not been able to correctly predict the charge transfer of insulator-insulator contacts [3]. For some polymers, the charge transfer has been observed to be independent of the work function of the metal in contact [28–30] , which renders it obstruct to assign an effective work function to the polymer.

3.1.2 Electron transfer

In early considerations on triboelectric charging, the charge transfer between insulators was attributed to electrons due to the relationship between the transferred cahrge and the work function of the metal in metal-insulator contact [3]. The participation of electrons in insulator-insulator contacts has been later supported by for example by Liu and Bard: by analysing the chemical reactions due to the residual charge on polymer surfaces, they suggested that the negative charge on the surfaces was due to electrons [31]. Opposing this deduction, Piperno *et al.* pointed out that the results of Liu and Bard can be explained by material transfer occurring in an experiments with such soft materials [32].

A common theoretical argument against the electron transfer model is the insufficient thermal energy to release an electron from the valence band of an insulator and introduce it to the conduction band of another. Ideally, the valence band of an

insulator is completely filled, and there is a large band gap (The difference of the energies of the highest occupied molecular orbital and the lowest unoccupied molecular orbital) where there is no available energy states for electrons to accommodate into. [3, 4]

For explaining the charge transfer between identical insulators, Lowell and Truscott [33] proposed that there are spatially localized high-energy states on insulator surfaces, accommodated by electrons 'trapped' to them. The depletion of occupied states per surface area could also account for the charge transfer between identical insulators. This theory has since been adopted by Lacks and Levandovski to explain the tendency of small particles to charge negatively when in contact with larger particles [34].

It is indeed reasonable that on insulator surfaces, the energy states of electrons are different than in the bulk. As discussed for example by Lacks and Sankaran *et al.*, the band theory of solids is only an strongly idealized approximation [4]. It does not account for energy states available on surfaces - in fact, the theory applies only for large, homogeneous systems.

However, not much effort has been done to explain the exact origin of these 'trapped' electrons. In insulators, electron transfer usually occurs between a pair of suitable molecular orbitals. In most organic polymers for example, there is no suitable functional groups for accepting or donating electrons [3]. However, the presence of electron donors and acceptors in polymers may be explained by scission of polymer chains, as discussed next.

3.1.3 Charge transfer between polymers

In recent years, progress has been made in understanding the triboelectric charging of polymers by becoming aware of the role of mechanoradicals, -cations and -anions in the charge transfer. Using Kelvin force microscopy, Bayetkin *et al.* found that when two polymer surfaces are pressed together and separated, the resulting charge is arranged in random mosaic patterns of oppositely charged regions on both surfaces. [35]. Similar results were obtained by Burgo et al. for frictional contact between teflon and polyethylene. [36]

Both groups considered their observations to be due to the scission of the polymer chains, which results in cationic, anionic or radical heads of polymer chain ends on

the surfaces. This type of chain scission has been earlier observed by Sakaguchi *et al.* [37,38], but it was associated to the triboelectric charging only after the findings of the other groups.

Due to the chain scission, material transfer is also involved in contact charging of polymers in some extent [35]. As mentioned by Williams [39], in soft polymers chain scission does not require a high friction or pressure, as the polymer chains on the opposite surfaces become entangled anyhow.

The presence of scissioned chain ends could account for electron transfer: For example, cationic and anionic chain heads on different surfaces could exchange electrons. If there is difference between bonding energies on the surfaces, a net charge transfer would occur. The depletion of available donors and acceptors could also explain the charge transfer between similar materials. [38]

The participation material transfer makes the contact electrification an even more complicated phenomenon. For example, Bayetkin *et al.* found that the polarity of the charging reverses for certain polymer pairs after a while [35]. They addressed this to the coating of the polymer particles with the other type of polymer: after numerous contacts, the particles acquired patches of the other polymer on their surface. It was proposed that these patches act effectively like the surface of the other polymer when in contact.

In the experiments presented in this work, polyethylene particles were fluidized in a glass container: thus there is no such entanglement of polymer chains as would be in a contact of two polymers. Still, the scission of the carbon chains is considered possibly influential: through numerous contacts with each other, the particles will acquire radical, cationic and anionic chain ends on their surface. It is supposed that these chain ends may contribute to both electron and ion transfer, with ion transfer being prominent in the present work.

3.1.4 Ion transfer and effect of relative humidity

Ion transfer is a the favoured mechanism for the triboelectric charging in a large review by McCarty and Whitesides [3]. One main argument supporting ion transfer is that the polarity of the charge transferred from surfaces which possess covalently bond ions and mobile (loosely bound) counterions correlates strongly with the sign

of the mobile ions. It is suggested that the mobile ions are transferred in contacts of such surfaces [40].

In the case of insulators with no mobile ions (like polyethylene), the charge transfer could be subject to ions originating from the environment. These ions would favorably adhere to the other of two surfaces. In particular, hydroxide (OH^-) ions present in water layers on solid surfaces is suggested to account for the charge transfer when the surfaces itself lack mobile ions. The charging due to separation of hydroxide ions gains support from molecular dynamics simulations reporting that in aqueous solutions, hydroxide ions accumulate on hydrophobic surfaces [41, 42]. [3, 43]

It is considered that the adsorption of the hydroxide may affect the results obtained in this study: as the hydrophobic polyethylene comes into contact with the hydrophilic glass surface in presence of a water layer, a net transfer of hydroxide to the polyethylene is expected. This could explain the negative net charge observed on polyethylene particles in a moderate humidity, as discussed in the results section.

The possible effects of the water layers on the surfaces are extensively discussed by McCarty and Whitesides [3], and are not repeated here. Most importantly in high humidities, water layers on insulating surfaces increase ionic conductivity, allowing charge accumulated on the surfaces to spread and discharge. The adsorbed water also allows charge transfer over longer distances (along liquid bridges formed between contacting surfaces) and lowers the electric potential difference at the separation stage (due to the high electric permittivity of water).

To consider the effect of the relative humidity, it is beneficial to estimate the amount of water adsorbed on the surfaces. By studying a water layer adsorbed on a silicon dioxide surface in room temperature, Asay and Kim [44] found that water forms an immobile, ice-like structure on the surface up to a thickness of three monolayers of water (9 nm). This stable configuration is considered to be due to the immobile hydroxyl groups on the surface. In the humidity range of 30..60 % RH, the topmost water layers begin to act like liquid. In even higher humidities, the thickness of the liquid water layer increases exponentially. [44]

It is supposed that a similar structure structure forms also on the glass surface used in the experiments. This would explain low charge-to-mass ratio in a high humidity, which is a general result in tribochargign experiments [3]. It is assumed that ionic conductivity of the water becomes significant when there is a mobile layer of liquid

on the surface in $RH \gtrsim 60$ %. On the contrary, ionic conductivity due to water on hydrophobic polyethylene particles is not expected to be significant in $RH \lesssim 60$ %.

3.1.5 Surface state theory

The surface state theory attributes the charge exchange between two surfaces to the effective work function difference between the surfaces. Although the term 'effective work function difference' is initially related to the electron transfer model, it applies conceptually for ion transfer as well. [45, 46]

The surface state theory has two limits basing on the density of available energy states for the charge carriers, namely the high density limit and and the low density limit. In the low density limit, charge carriers are transferred from initially occupied states of the other surface to the lower energy states of the other. Equilibrium is achieved as the states on the both surfaces become filled up to an equal energy level. If the charge of each carrier is that of electron ($-e$) and the number of surface states per unit energy per unit area on both surfaces is N, the charge transferred per unit area is

$$\sigma_{12} = -eN(\varphi_1 - \varphi_2), \tag{3.1}$$

where φ_1 and φ_2 are the highest energy levels occupied before the contact. The difference between the energy levels φ_1 and φ_2 is interpreted as the effective work function difference between the surfaces. [46]

It is apparent how Equation 3.1 is to be modified if the charge of each carrier differs from the charge of an electron or the number of states per unit energy differ between the surfaces. However, the equation becomes complicated if the density of surface states per unit energy is not constant.

In the high density limit, the energy of the charge carriers is affected by the electrostatic potential due to the total charge transferred. In this situation, the net charge transfer per unit area is

$$\sigma_{12} = -\varepsilon\frac{(\varphi_1 - \varphi_2)}{ez}, \tag{3.2}$$

where ε is the electric permittivity between the surfaces and z is the distance between the surfaces. [46]

Equation 3.2 can be derived by considering the surfaces as uniformly charged parallel

plates and balancing the total energy (electrostatic potential energy + the effective work function difference) of the charge carriers on the opposite surfaces. The electric potential between the surfaces increases as z increases, causing the transferred charge to flow back when the surfaces are separated. The final charge exchange after separation of the surfaces is dictated by the critical distance z_c over which the charge can transfer. For electrons, this distance could be the maximum tunneling distance, which is order of few nanometers. [3]

3.2 Charge transfer model

The charge transfer model used in this study stems from the high density limit described in the previous section. As discussed before, there may be be several different charge transfer mechanisms involved. However, the surface state theory is formulated only for transfer of one type of charge carrier. At this point, it is assumed that the model describes the net charge transfer between surfaces in certain conditions, although multiple types of charge carriers may be present.

Schein *et al.* [47] introduced following equation to describe charge exchange between two insulating surfaces in contact:

$$\sigma_{ij} = \frac{\varepsilon}{z_c e} \left(\varphi_i - \varphi_j - z_c e E_{ij} \right), \tag{3.3}$$

where σ_{ij} is the charge transferred from surface j to surface i per unit area, ε is the permittivity of the medium, z_c is the critical distance over which the charge can transfer, e is the elementary charge, φ_i and φ_j are the effective work functions of the surfaces and E_{ij} is the external electric field strength at the contact point (pointing from surface j to surface i).

The external electric field accounts for the electric field due to the charge accumulated on the surfaces and acts as a limiting factor for the charge transfer. This is further discussed in the next section.

Basing on Equation 3.3, Ali *et al.* developed an iterative method to model the charge exchange of a disperse system of spherical powder particles [48]. Following them, Laurentie *et al.* developed a numerical formulation of Equation 3.3 suitable for calculating the charge transfer between discrete particles in a vibrated bed [49, 50]. This model has since been applied to simulate triboelectric charging in a fluidized

bed for example by Kolehmainen *et al.* [19].

The discrete formulation given by Laurentie et. al [49, 50] expresses the amount of charge transferred between two consecutive time steps. Accroding to them, charge transfer between two particles can be formulated as

$$\frac{\Delta q_{ij}}{\Delta A_{ij}} = \varepsilon \left(\frac{\Delta \varphi_{ij}}{z_c e} - E_{ij} \right), \tag{3.4}$$

where Δq_{ij} is the charge transferred from particle j to particle i during a time step, ΔA_{ij} is the change in contact area, ε is the permittivity of the medium and $E_{ij} = \mathbf{E}_{ij} \cdot \mathbf{n}_{ij}$ is the electric field strength at the contact point (pointing from j to i).

As suggested by Laurentie *et al.*, charge transfer in the numerical model is limited to the period during which the contact area is increasing ($dA_{ij}/dt > 0$). As long as the normal overlap distance of particles in contact is small, the total charge transferred during a contact depends only on the maximum contact area $A_{\max}$ by [19]

$$\Delta q_{ij} = A_{\max} \varepsilon \left(\frac{\Delta \varphi_{ij}}{z_c e} - E_{ij} \right). \tag{3.5}$$

The advantage of linking the charge transfer to the change of the contact area is the easiness of implement the charge transfer model among the soft-sphere contact model utilized in CFD-DEM simulations. The contact area of the colliding objects can be approximated as [19]

$$A_{ij} = 2\pi \delta_{ij} r^*. \tag{3.6}$$

As the normal intersection and the equivalent radius are already calculated for evaluating the soft-sphere model, it is a matter of one line of code to calculate also the contact area.

In practice, the change of the contact area is obtained by tracking the contact area of each ongoing contact and calculating the difference between two successive time steps. Tracking the contact area does not increase the complexity of the implementation much, as collision data of individual collisions is already recorded for numerically integrating the tangential displacement of each ongoing contact.

3.3 Softness correction and acceleration factor

Lowering the Young modulus in order to achieve feasible simulation times increases the maximum contact area of the collisions, which in turn affects the total charge transferred. By considering the energy balance of a Hertzian spring, Kolehmainen *et al.* concluded that the ratio of the charge transferred in a contact is proportional to $(Y^*)^{5/2}$, if the initial relative velocities are unaltered and the coefficient of restitution is taken to be unity. The ratio of the charge transferred in a real contact to the charge transferred in a simulated 'soft' contact is thus

$$a_{\text{corr}} = \frac{\Delta q_{\text{real}}}{\Delta q_{\text{soft}}} = \left(\frac{Y^*_{\text{soft}}}{Y^*_{\text{real}}} \right)^{2/5} . \tag{3.7}$$

According to Kolehmainen *et al.*, the effect of particle softening on the charge transfer can be corrected by multiplying the charge transferred at each time step by a_{corr}. If the charge transfer rate is further scaled by a arbitrary acceleration factor a, the ratio of the simulated and real charge transfer rates is also scaled by a.

By running trough several simulation cases with varying values of Y^*, Kolehmainen *et al.* deduced that accelerating the charge transfer rate alters the charge distribution among the particles, but the saturation charge is relatively unaltered. If the simulation time is scaled afterwards by a, the evolution of the total charge is similar between cases run with different acceleration factors. Thus the artificial acceleration factor a can be used to reduce the total simulation time without considerably affecting to the saturation charge [19].

3.4 Equilibrium charge and saturation charge

The charge accumulated on a particle is limited by the electric field induced by the charge on particle itself and by the external electric field. Considering an isolated particle in contact with wall and basing on Equation 3.4, no charge is transferred when

$$\frac{\Delta\varphi}{z_c e} = E_{\text{ext}} + \frac{q}{\pi\varepsilon D^2}, \tag{3.8}$$

where $\Delta\varphi$ is the effective work function difference between the particle and the wall. The electric field at the contact point is split into the contributions of the external electric field E_{ext} and the field due to the charge q of the particle.

When the electric field due to the particle itself prevents further charge transfer, the particle has acquired equilibrium charge q_{eq}. Substituting $q = q_{\mathrm{eq}}$ and $E_{\mathrm{ext}} = 0$ in Equation 3.8 gives

$$q_{\mathrm{eq}} = \pi \varepsilon D^2 \frac{\Delta\varphi}{z_c e}. \tag{3.9}$$

In a bed with conducting walls, the equilibrium charge is half of that given by Equation 3.8 due to the image charge induced on the wall [19].

The effect of external electric field on triboelectric charging has been studied for example by Mizutani *e*t al. [51]. They found that the charge-to-mass ratio of particles travelled over an inclined, vibrated plate has a linear relationship with the applied electric field. This is in line with Equation 3.8, which suggest a linear relationship between the charge accumulated on particles and the applied field (taken that the number of particles is small so that they do not contribute to the electric field experienced by each other).

To characterize the strength of electrostatic effects in a fluidized bed, Kolehmainen *et al.* compared the magnitude of the gravitational force to the magnitude oif electrostatic force between two oppositely charged particles in contact. If the magnitude of the charge on both particles is q_{eq} and diameter of both particles is D, the ratio of the magnitudes of electrostatic and and gravitational forces is

$$e/g = \frac{q^2/(4\pi\varepsilon D^2)}{mg}, \tag{3.10}$$

where $e = q_{\mathrm{eq}}/(m\pi\varepsilon D^2)$ is the electrostatic force per particle mass (not to be confused with the elementary charge) and g is the gravitational acceleration. Substituting Equation 3.9 into Equation 3.10, one obtains

$$e/g = \frac{\pi\varepsilon D^2}{4mg}\left(\frac{\Delta\varphi}{z_c e}\right)^2. \tag{3.11}$$

It should be noted that the value of e/g given by Equation 3.11 if four times greater than e/g for conducting wall, as the respective equilibrium charges diffes by a factor of two.

In dense systems, the particles do not generally acquire a charge as high as the equilibrium charge, but the charge saturates at a lower level. This is referred as the saturation charge (q_∞) in line with Kolehmainen *et al.* [19]. The saturation charge

is limited by the total electric field, which is affected by both the charge of the particles and charge on the wall.

As discussed by Kolehmainen *et al.* [19], the time evolution of the total charge Q in the bed is expected to obey

$$Q = Q_\infty \left(1 - e^{-kat}\right), \tag{3.12}$$

where Q_∞ is the saturation charge of the whole bed, a is the acceleration factor and k is a coefficient depending on the intensity of particle-wall collisions. In the results section, the saturation charge given by Equation 3.12 will be compared to the experimentally measured total charge of the particles.

Generally, both the equilibrium charge and the saturation charge depend on the maximum charge transfer distance z_c and the effective work function difference $\Delta\varphi$. In this study, it was not regarded reasonable to choose a strict value for z_c, as the values found in literature range from 1 nm to 500 nm. Basing on Equation 3.4, the charge transferred in a single contact depends only on the lumped parameter $\Delta\varphi/(z_c e)$. This is regarded as the electric field strength required to counterbalance the influence of the effective work function difference.

In the sake of generality, the effective work function differences used in the simulations are expressed in terms of $\Delta\varphi/(z_c e)$ instead of first choosing separate values value for z_c and $\Delta\varphi$. For convenience, the lumped parameter $\Delta\varphi/(z_c e)$ is referred as the effective work function difference from now on.

The relation of the effective work function difference and the accumulated charge in the bed is not known *a priori*, as it is affected for example by the geometry and the dynamics of the bed. Thus preliminary simulations are required. The effective work function differences used in preliminary simulations are chosen basing on Equation 3.11 to match with reasonable values of e/g .

3.5 Electric field and force on particles

In insulating materials (like polyethylene and glass used in this study), the charge transferred in a single contact is supposed to reside on the contact area. As the particles gain charge through numerous contacts, it is approximated that after a while the charge is uniformly distributed on the particle surface. Therefore the

charge on a spherical particle can then be approximated as a point charge localized at the center of the particle. This approximation is used for example by Laurentie *et al.* [49, 50] and Kolehmainen et al. [15, 19].

As discussed later, the charge transfer in the simulations must be artificially accelerated to reach reasonable simulation times. This renders the approximation of uniformly charged particle surfaces actually welcome; effectively, it distributes the charge obtained in one contact like the charge was accumulated through numerous contacts.

A hybrid method introduced by Kolehmainen *et al.* [15, 19] is used to calculate the electric field affecting on each particle. In the method, the total field is divided into a short-range field and a long-range field. A correction term is used to remove the overlapping contributions of the short-range and long-range terms. Following Kolehmainen *et al.*, the electric field affecting on particle i can be expressed as

$$\mathbf{E}_i = \mathbf{E}_{s,i} + \mathbf{E}_{\nabla^2,i} + \mathbf{E}_{c,i}, \tag{3.13}$$

where $\mathbf{E}_{s,i}$ is the short-range term, $\mathbf{E}_{\nabla^2,i}$ is the long-range term and $\mathbf{E}_{c,i}$ is the correction term.

The short-range field is evaluated as a sum of electric fields of the particles in the vicinity of particle i as

$$\mathbf{E}_{s,i} = \frac{1}{4\pi\varepsilon} \sum_j q_j \frac{\mathbf{x}_i - \mathbf{x}_j}{|\mathbf{x}_i - \mathbf{x}_j|^3}, \tag{3.14}$$

where ε is the electric permittivity of the medium and q_j is the charge of particle j. The sum runs over all particles belonging to the neighbourhood of particle i.

Kolehmainen *et al.* employed a cut-off radius to restrict the range of the short-range term. In this work, the short-range field is instead evaluated between a particle pair if both particles belong either to the same computational cell or so-called *interacting cells*. This is convenient to implement, as in `OpenFOAM` the cell occupancy of particles is already tracked in order to couple the motion of the particles and the carrier phase.

The concept of interacting cells in `OpenFOAM` is described in Figure 3.1. The list is constructed by first expanding the bounding box of each cell by a given maximum interaction distance R. If the expanded bounding boxes of two cells overlap, it is

deduced that the particles in these cells possibly interact. To evaluate the possible interactions during the simulation, the other of the cells is added to the interaction list of the another.

To avoid double counting, any cell B in the range of cell A is added to the interaction list of cell A only if the index of B is greater than the index A. This is illustrated by the arrows on the cell interfaces in Figure 3.1. The interactions between particle are evaluated by following algorithm, which is slightly modified from the original implementation in standard OpenFOAM:

- Loop through each cell A in the computational domain
  - Loop through each particle p_A in cell A
    - Loop through each interacting cell B of cell A
      - Loop through each particle p_B in cell B
      - Evaluate interaction between particles p_A and p_B.
    - Loop through each particle p_{A2} in cell A
      - Evaluate interaction between p_A and p_{A2}, avoiding double counting.

As only the cells with greater index are listed in the interaction lists of a certain cell, interaction between each particle pair will be evaluated only once. For particles in the same cell, the double counting is prevented by comparing the pointers of the particles. The evaluation of the short-range electric field and the charge transfer are subsumed into the original implementation of the soft-sphere contact model of OpenFOAM.

As mentioned before, the evaluation of the short-range term is not strictly restricted to the particles in some critical radius, as the evaluation of the term is not a demanding task after calculating the distance between the two particles. Instead, the short-range field is calculated between all the particles in interacting cells. The maximum interaction distance R used to construct the interaction lists serves as the minimum distance of the short-range field, while the maximum distance is limited by the size of the interactign cells.

The long-range field is calculated as the gradient of the electric potential ϕ:

$$\mathbf{E}_{\nabla^2} = -\nabla\phi. \tag{3.15}$$

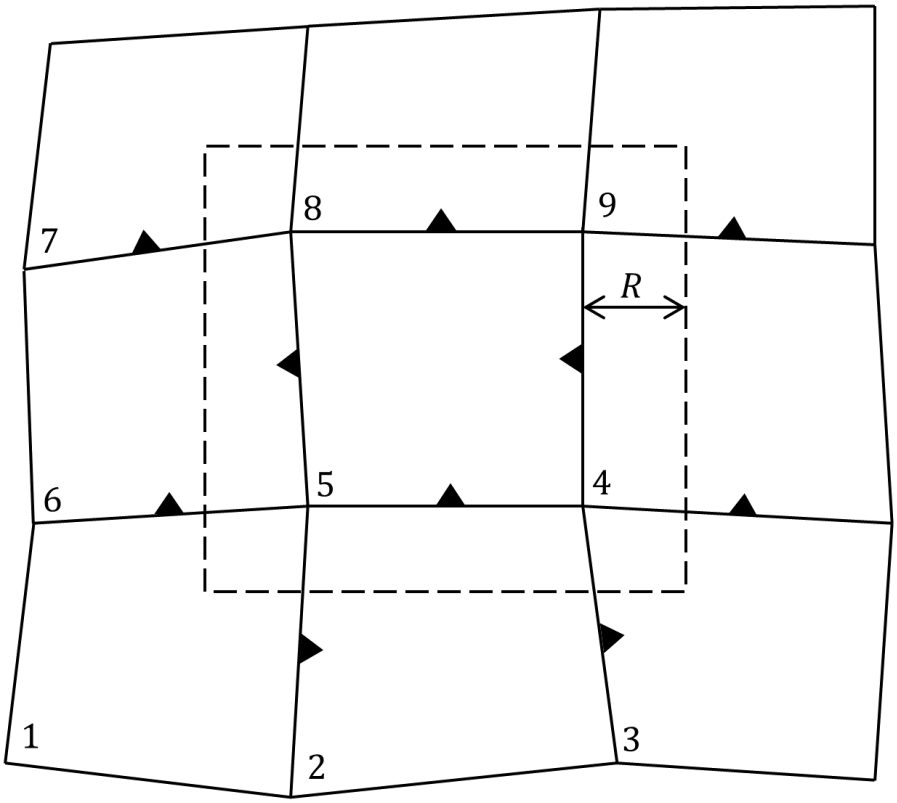

Figure 3.1 *Interacting cells of cell 5. R is the maximum interaction distance, defining the size of the bounding box (dashed line). The arrows on the cell interfaces indicate how the interaction lists are organized: for example, cells 2 and 6 belong to the interaction list of cell 1.*

The electric potential, in turn, is solved a from a Poisson equation

$$\nabla^2 \phi = -\frac{\rho_q}{\varepsilon}, \tag{3.16}$$

where ρ_q is the charge density obtained by dividing the total charge in each cell with the cell volume.

The correction term is used to remove the overlapping contribution of the long-range field with the short-range field. According to Kolehmainen *et al.* the correction term for particle i is

$$\mathbf{E}_{c,i} = -\frac{1}{4\pi\varepsilon} \sum_j q_j \frac{\mathbf{x}_{\text{cell},i} - \mathbf{x}_{\text{cell},j}}{|\mathbf{x}_{\text{cell},i} - \mathbf{x}_{\text{cell},j}|^3}, \tag{3.17}$$

which approximately gives the contribution of particles considered in the short-range term to the long-range term in the cell of particle i.

As the correction term covers all the particles in interacting cells, it is dependent on the total charge and the position of the interacting cells. What is more, the correction term is equal among all the particles in a certain cell.

It is reasonable to correct the long-range term obtained from Equation 3.15 before assigning the field to the particles, instead of assigning the field first and correcting the field of each particle individually. Basing on Equation 3.17, the correction term for any cell A becomes

$$\mathbf{E}_{c,A} = -\frac{1}{4\pi\varepsilon}\sum_{B} Q_B \frac{\mathbf{x}_A - \mathbf{x}_B}{|\mathbf{x}_A - \mathbf{x}_B|^3}, \tag{3.18}$$

where the sum goes over all the interacting cells of cell A. Q_B is the total charge of cell B and $\mathbf{x}$ indicates the location of the cell center indicated by the subscript. In principle, the correction term removes the contribution of the interacting cells from the long-range field of each cell.

3.6 Electric field on a dielectric surface

The net charge accumulated on particles originates from the walls around. If the electric conduction and other means of charge dissipation are neglected, an opposite charge remains on the wall surfaces. Thus a boundary condition considering the surface charge is necessary to correctly calculate the electric field inside the bed. Although not considered in the simulations, also the polarization of the dielectric walls contributes to the electric field.

3.6.1 Surface charge density

The surface charge density σ_f on a particular face f on the wall can be considered as the average charge density on the face,given as

$$\sigma_f = \frac{1}{A_f}\int_{A_f} \sigma dA, \tag{3.19}$$

where A_f is the are of the face. This is a similar approximation than assuming the charge on the particles to be uniformly distributed on their surfaces.

In the lagrangian particle tracking libraries of OpenFOAM, collisions between individual particles and the faces forming up the wall are tracked. In each contact, the

charge transferred from wall to the particle leaves behind an opposite charge on the wall, which is considered by the surface charge density σ_f of a particular face f:

$$\Delta\sigma_f = -\frac{\Delta q}{A_f}, \tag{3.20}$$

where $\Delta\sigma_f$ is the change of the surface charge density, δ_q is the charge transferred from the wall to a particle and A_f is the area of the face.

As the charge on insulator surfaces is strictly localized (at least when no liquid films present), the charge transferred in a contact depends on if the point of contact has already been subject to a contact. On a planar face however, the average charge density is directly proportional to the average electric field strength perpendicular to the face (from Gauss's law). Thus statistically, using the average charge density for calculating the electric field should not contribute to the charge transfer over a long period.

3.6.2 Gauss's law and polarization

The Gauss's law of electrostatics describes how the electric flux over a closed surface is related to the total charge enclosed by the surface. For a closed surface S,

$$\int_S \mathbf{E} \cdot \mathbf{n}\, dS = \frac{Q}{\varepsilon_0}, \tag{3.21}$$

where $\mathbf{E}$ is the electric field, $\mathbf{n}$ is an unit normal pointing outwards from the surface, Q is the total electric charge enclosed and ε_0 is the vacuum permittivity. This fundamental equation is valid in all materials, as the total charge includes both free charge and the charge bound to the atoms or molecules of the medium. [52, 53]

The problem of using Equation 3.21 is that the polarization of the charges bound to the atoms or molecules is unknown. However, the total charge enclosed in a volume can be separated into the charge due to polarization and the free charge [53]:

$$Q = Q_{\text{free}} + Q_{\text{pol}}. \tag{3.22}$$

The total charge due to polarization inside the surface S is obtained by integrating

the inwards-pointing polarization density $\mathbf{P}$ over the surface. This results in

$$Q_{\text{pol}} = -\int_S \mathbf{P} \cdot \mathbf{n} dS \tag{3.23}$$

Substituting Equation 3.23 into Equation 3.21 and rearranging gives

$$\int_S (\varepsilon_0 \mathbf{E} + \mathbf{P}) \cdot \mathbf{n}\, dS = Q_{\text{free}}. \tag{3.24}$$

In linear, homogeneous, isotropic, non-dispersive materials the polarization density is proportional to the electric field through $\mathbf{P} = \chi \varepsilon_0 \mathbf{E}$, where the electric susceptibility χ is related to permittivity of the material through $\varepsilon = (1 + \chi)\varepsilon_0$ [52]. Now a more familiar equation describing the electric field is obtained:

$$\int_S \varepsilon \mathbf{E} \cdot \mathbf{n}\, dS = Q_{\text{free}}. \tag{3.25}$$

Utilising divergence theorem, the differential form becomes

$$\nabla \cdot \varepsilon \mathbf{E} = \rho_{\text{free}}, \tag{3.26}$$

where ρ_{free} is the free charge density [52]. If the permittivity is constant, this reduces to

$$\nabla \cdot \mathbf{E} = \frac{\rho_{\text{free}}}{\varepsilon}. \tag{3.27}$$

This is essentially same as Equation 3.16, where it is implicitly assumed that the permittivity is constant in the region of interest and the effect of polarisation is neglected.

In this work, the computational mesh is split into two regions: the bed containing the fluid and a surrounding region. The electric potential is individually solved from Equation 3.16 for both regions, setting the potential zero at the boundaries of the surrounding region (far enough to not contribute to the electric field in the bed). Although the implemented boundary condition allows setting different permittivity for each region, vacuum permittivity is used in both regions, thus neglecting the effect of polarization.

3.6.3 Effect of surface charge

Enclosing an interface of two dielectric media with a control surface S as in Figure 3.2 and applying Equation 3.25 results in

$$-\mathbf{n}_{AB} \cdot (\varepsilon_A \mathbf{E}_A - \varepsilon_B \mathbf{E}_B) = \sigma, \tag{3.28}$$

where electric fields $\mathbf{E}_A$ and $\mathbf{E}_B$ at the different sides of the interface are assumed to be constant and $\mathbf{n_{AB}}$ is a unit normal vector perpendicular to the interface, pointing from A to B. The surface charge density σ accounts for the free charge enclosed by the control surface and the flux parallel to the interface is neglected. [52]

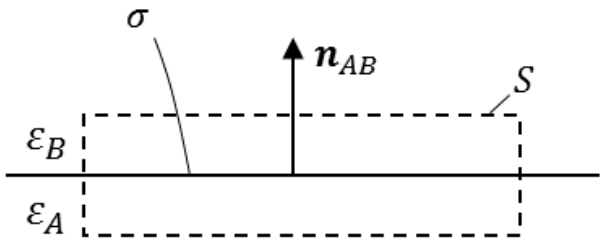

Figure 3.2 *An interface of dielectric media with permittivities ε_A and ε_B and surface charge density σ enclosed by a fictitious surface S.*

The boundary conidition for a dielectric interface with surface charge is implemented by utilising the `mixed` boundary condition of `OpenFOAM`, which is a weighted combination of fixed gradient and fixed value boundary conditions. The actual implementation is based on `turbulentTemperatureCoupledMixedFvPatchScalarField`, which is a boundary condition for heat transfer between fluid and solid regions. All in all, the boundary condition is very similar to a heat conduction boundary condition between regions of different thermal conductivities.

Consider two cells sharing a common boundary face at the interface of two regions such as in Figure 3.3. Let the electric potential at the common face be ϕ_f. Applying Equation 3.28 and assuming that the potential changes linearly from the face towards the cell centers gives

$$\varepsilon_A \frac{\phi_f - \phi_A}{d_A} + \varepsilon_B \frac{\phi_f - \phi_B}{d_B} = \sigma_f, \tag{3.29}$$

where ϕ_A and ϕ_B are potentials at the cell centers and d_A and d_B are the normal

distances from the boundary face to the cell centers. Solving for ϕ_f results in

$$\phi_f = \frac{\frac{\varepsilon_A}{d_A}\phi_A + \frac{\varepsilon_B}{d_B}\phi_B + \sigma_f}{\frac{\varepsilon_A}{d_A} + \frac{\varepsilon_B}{d_B}}. \tag{3.30}$$

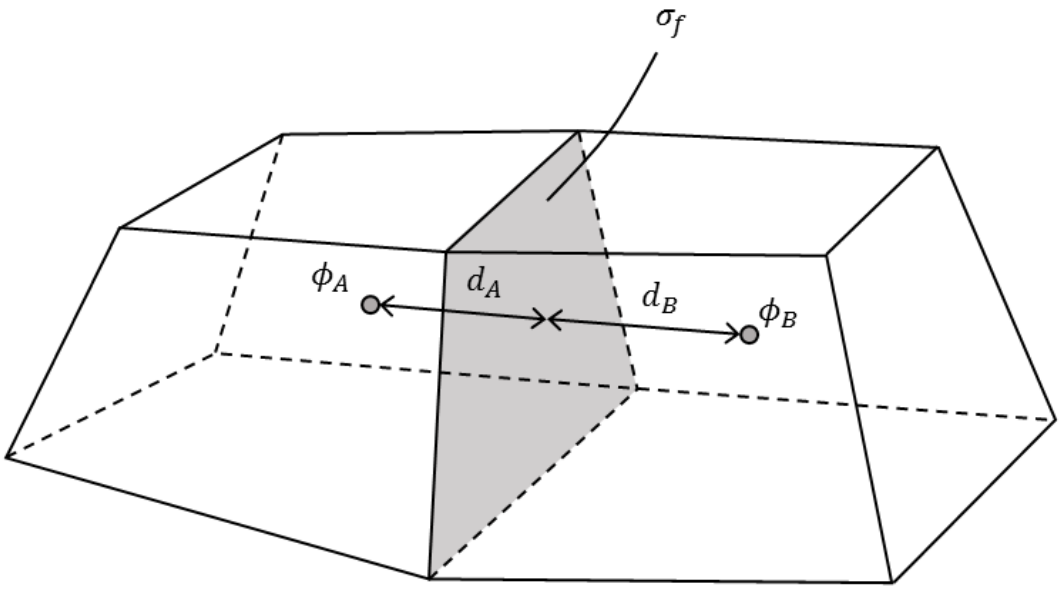

Figure 3.3 *Two cells sharing a common face at the interface of two dielectric media (gray color). The electric potential at the boundary face is solved according to the permittivities of the cells and the potentials at the cell centers.*

In framework of the mixed boundary condition of OpenFOAM, the value at the boundary face is calculated by a weighted sum of the results that would be given by fixed gradient and fixed value boundary conditions. For cell A then

$$\phi_f = a\phi_{\text{ref}} + (1-a)\left(\phi_A + (\nabla\phi \cdot \mathbf{n}_{AB})_{\text{ref}}\, d_A\right), \tag{3.31}$$

where a is the weighting factor of the fixed value boundary condition, ϕ_{ref} is the reference for the fixed value and $(\nabla\phi \cdot \mathbf{n}_{AB})_{\text{ref}}$ is the gradient pointing outwards from cell A. By comparing Equations (3.30) and (3.31), one finds that the desired values are

$$a = \frac{\frac{\varepsilon_B}{d_B}}{\frac{\varepsilon_A}{d_A} + \frac{\varepsilon_B}{d_B}}, \tag{3.32}$$

$$\phi_{\text{ref}} = \phi_B \tag{3.33}$$

and

$$(\nabla\phi \cdot \mathbf{n}_{AB})_{\text{ref}} = \frac{\sigma_f}{\varepsilon_A}. \tag{3.34}$$

This boundary condition applies for interfaces of dielectrics with different permittivities, but as mentioned, vacuum permittivity is used for both the internal and the external region. Hence the polarization of the dielectric wall is not considered in this study.

3.6.4 Points to develop

As the contact area given by Equation 3.6 is proportional to the normal displacement, the charge is transferred only if the normal displacement of the colliding objects is subject to change. This neglects the contribution of rolling and sliding of the surfaces over each other: for a rolling sphere for example, Equation 3.6 would give no charge transfer.

The rate of area introduced through sliding or rolling could be calculated simply as the product of the slip velocity and the diameter of the contact area; basing on Equation 3.6, the rate of change of the total contact area would be

$$\frac{dA_{ij}}{dt} = 2\pi r^* \frac{\delta_{ij}}{dt} + \sqrt{8\delta_{ij} r^*}|\mathbf{v}_{ij}^t|. \tag{3.35}$$

This factor could be rather easily implemented to the charging model, but is not yet used in this study. It is not considered to be a crucial factor for predicting the saturation charge in a fluidized bed as the saturation charge is ultimately limited by the electric field, which is not directly affected by the rate of charge transfer nor by the rate of change of the contact area.

The electric permittivity of the medium is used when calculating both the long-range and short-range electric fields. An effective medium approximation could be introduced in the simulations to approximaely account for the polarization of the particles. For example, the Bruggeman equation relates the effective permittivity ε_m of the medium to the permittivities of the carrier phase (ε_c) and dispersed phase as (ε_s) as

$$\alpha = \frac{\varepsilon_s - \varepsilon_m}{\varepsilon_s - \varepsilon_c} \left(\frac{\varepsilon_c}{\varepsilon_m}\right)^{1/3}, \tag{3.36}$$

where α is the volume fraction of the carrier phase. [54].

It is considered that the effective medium approximation could improve the accuracy to the results, as it would affect the electric field and hence the charge transfer predicted by the triboelectric charging model. Equation 3.36 must be solved implicitly, but a simple linear approximation could afford an explicit result accurate enough [54].

4. EXPERIMENTAL SETUP

Clear polyethylene particles (Cospheric, CPMS-0.96) were used in the fluidization experiments. Basing on a Certificate of Analysis (COA) provided by the manufacturer, at least 96 % of the particles belong to a size range of $250 - 300$µm and more than 95 % of them are spherical. A histogram describing the size distribution is given in Figure 5.2.

The main parts of the experimental setup are schematically depicted in Figure 4.1. The fluidizing device consists of a rectangular soda-lime glass pipe (A) and a plastic base part (B). The gas flows trough a removable plastic inlet (C) and leaves trough a conical expansion (D) at the top of the glass pipe. The inner dimensions of the pipe is 10 mm $\times$ 10 mm and the distance from the inlet to the outlet is 74 cm.

The flow inlet is a 6 mm $\times$ 6 mm square duct covered by a stainless steel grating with an opening of 63 μm. Both the glass pipe and the inlet part are removable, which enables collecting the particles from the bottom of the pipe after fluidization. The total charge on the particles was measured before and after fluidization using a Faraday cup connected to an electrometer (Monroe 284).

The flow rate of nitrogen used for fluidization is controlled by a mass flow controller (Bronkhorst, F201CV) calibrated for nitrogen. A part of the gas is conveyed trough a humidifier unit (E), while the other part is conducted directly into the base part. The portion of the gas flowing trough the humidifier is manually controlled with using a rotameter (F) and a ball valve (G).

The humidifier is based simply on evaporation of water from a free water surface to the surpassing flow. By keeping the humidifier in a mildly heated heat bath, the gas flown trough the humidifier is effectively saturated.

The temperature and the relative humidity are measured from the base part using a relative humidity/temperature transmitter (Omega HX94 SS RH Probe). As the

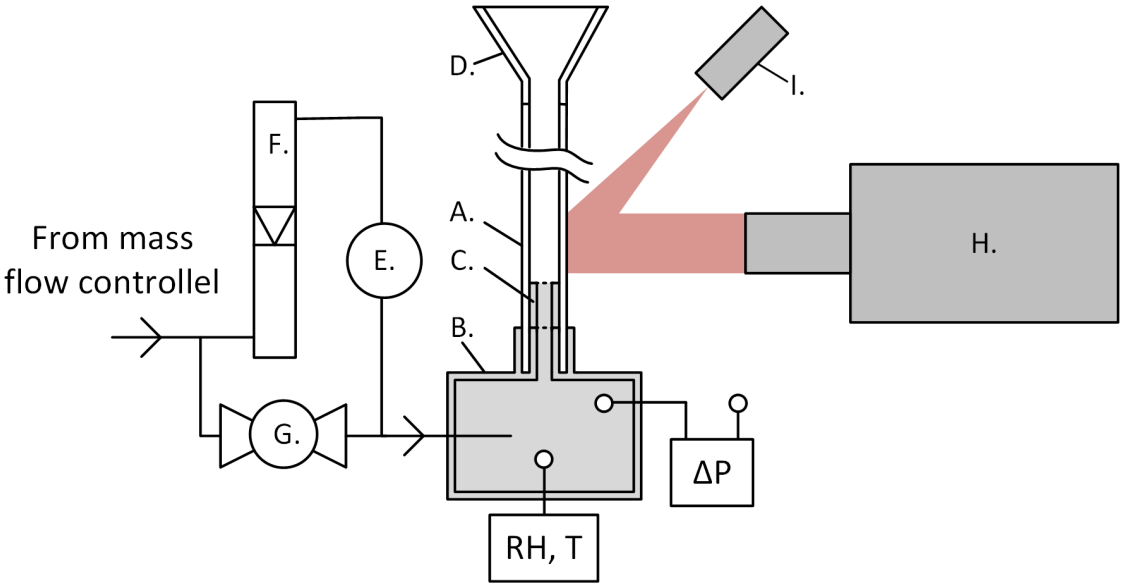

Figure 4.1 *The fluidizing device and the instruments used. A: glass pipe, B; base part, C: removable inlet, D: conical expansion, E: humidifier, F: rotameter, G: ball valve, H: high-speed camera, D: HF laser.*

gas flown trough the humidifier is saturated, the relative humidity conveyed to the bed is close to the ratio of the flow rate trough the rotameter to the total flow rate. The fine tuning of the humidity is done by adjusting flow resistance of the rotameter.

The pressure difference between the base part and the ambient air is measured by a differential pressure sensor (Sensirion SDP1108). The hydrostatic pressure difference due to the different densities of the nitrogen and the ambient air is insignificant (under 0.5 Pascals). Also the dynamic pressure difference in the base part and at the pressure outlet is considered to be negligible.: therefore the pressure sensor effectively measures the pressure drop due to the friction over the pipe and the fluidized bed.

To qualitatively examine adhering of particles on the wall, the wall layer of particles was pictured using a high-speed camera (pco dimax HS4) in some selected conditions. To limit the amount of pictures taken, the camera was set to take five successive pictures once per second at 0.5 ms intervals. The bed was illuminated at 45° angle with using a pulsed diode HF laser (Cavitar Cavilux HF), giving a 2 μs lasting pulse during each exposure cycle of the camera.

The image resolution of the camera is 2000 $\times$ 2000 pixels and the imaged area was adjusted to cover the range of 15..30mm above the bed inlet. PIVlab [55] was used

to estimate the velocity of the particles in the imaged area in terms of Particle Image Velocimetry. The interrogation window was set to be 128×128 pixels, respecting to a physical size of about three particle diameters. FFT window deformation (a Fourier transform correlation with multiple passes and deforming windows [55]) was used as the cross correlation method.

5. SIMULATION SETUP

The simulations were conducted utilising an application build onto an original OpenFOAM-application named `DPMFoam` (DPM = Discrete Particle Method), which is capable of coupling the motion of particles and a continuous phase. The appended application accounts for evaluating triboelectric charging, electric field and the electrostatic forces on the particles. The contribution of the author was to introduce the tracking of the surface charge of the walls and the respective boundary condition for dielectric interfaces as described in Section 3.6. Also the correction of the long-range electric field was modified to be conducted on per-cell basis.

5.1 Geometry and boundary conditions

The inner dimensions of the simulated bed match with the experimental bed and are given in Figure 5.1. An uniform velocity boundary condition was used at the inlet and a constant pressure boundary condition at the outlet. The flow inlet velocity was set according to the mass flow used in the experiments and no-slip condition was used on the walls. The density and viscosity were set to match with those of dry nitrogen at 24 °C.

The cell size of the computational mesh inside the bed is 1 mm^3, having thus dimensions of about 3 times larger than the maximum particle diameter. The same computational mesh is used for computing both the fluid dynamics and the electric potential. The maximum interaction distance between particles was set to 900 μm, which is slightly smaller than the average cell dimensions. In principle, all the particles in the nearest cells contribute to the short-range electric field of each particle.

To consider the effect of the surface charge, a cylindrical computational region is introduced around the bed. The boundary condition described in Section 3.6 is used for coupling the electric potential at the interface of the two regions. A fixed value boundary condition is used for the at the outer boundaries of the environmental

region. Vacuum permittivity is used as the permittivity of both the interior and the environmental region, thus ignoring the effects of polarization of the wall and the particles.

The dimensions of the surrounding region are given in Figure 5.1, which shows the cross section cross-section taken from a simulated case. The color scale shows the solution of the electric potential, indicating how the electric potential distributes smoothly from the interior of the bed to the surrounding region.

5.2 Time step and acceleration factor

The time step of the simulations is automatically adjusted during the simulation basing on the Courant number of the continuous phase. In addition to limiting the maximum Courant number to 0.5, the maximum time step is limited to 10^{-4} seconds. Furthermore, the evaluation of the contact model is conducted in an appropriate amount of sub-steps given by Equation 2.38. The acceleration factor used in the simulations is $a = 15$ if not otherwise stated.

The total simulation time in each case is limited to 2.0 seconds, as it is long enough for the total charge of the bed to nearly achieve saturation. When scaled by the acceleration factor, two seconds of simulated time corresponds to 30 seconds of real time with respect to the total charge accumulated in the bed.

5.3 Particle properties

Each simulation starts from an equal initial condition with 143500 initially uncharged particles, resulting in a mass of around 1.5 grams. The initial state was obtained by arranging the particles in a cubical grid and running a simulation without triboelectric charging for 2 seconds to achieve a full fluidization.

The particle size distribution used in the simulations is determined by the truncated normal distribution shown in Figure 5.2. The distribution has been fit to the number frequency distribution of particle size provided by the manufacturer. As seen from Figure 5.2, the fitted distribution with an expectation value of 277 μm and a standard deviation of 13.7 μm matches with the discrete distribution fairly well.

The material properties used in the simulations are given in Table 5.1. The real

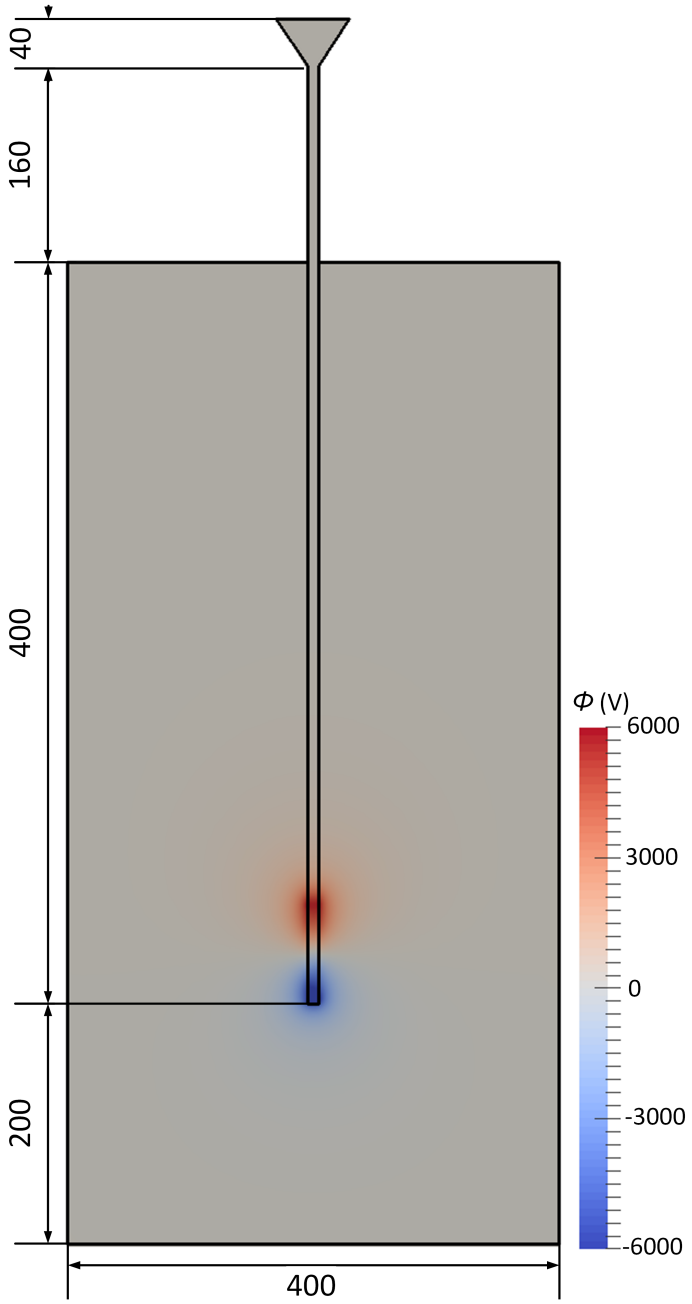

Figure 5.1 *A cross-section of the bed and the environmental region. The figure shows a snapshot from a simulation, depicting the long-range electric potential calculated from Equation 3.16.*

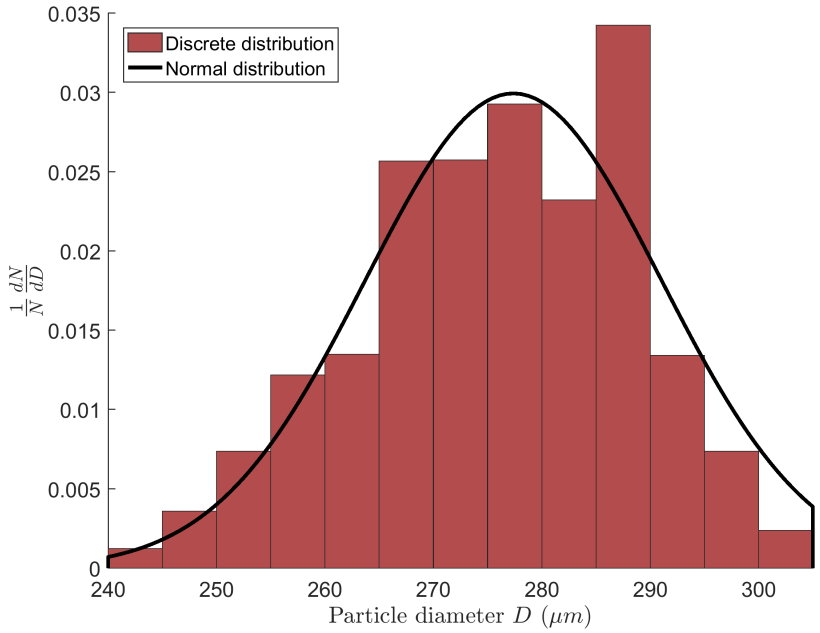

Figure 5.2 *The discrete particle size distribution and the truncated normal distribution used in the simulations. According to the discrete distribution, the normal distribution is truncated at 240 and 305 μm.*

values for the Young moduli given in the table the range of values found in literature. The equivalent Young's modulus and the equivalent shear modulus are calculated according to the definitions given in Equation 2.36. The resulting equivalent moduli for both particle-wall and particle-particle contacts are given in Table 5.2. The friction coefficient was set to 0.3 for both particle-particle and particle-wall contacts.

Table 5.1 *The material properties used in the simulations and the range of real values.*

Property	Polyethylene		Glass	
	Simulation	Real	Simulation	Real
Y (MPa)	0.5	500..1200	0.5	50 000..90 000
ν	0.46	0.46	0.22	0.22

Table 5.2 *The resulting Young moduli and the shear moduli for both contact types with the respective charge transfer corrections.*

Property	Particle-particle		Particle-wall	
	Simulation	Real	Simulation	Real
Y^* (MPa)	0.31	320 .. 760	0.31	630 .. 1500
G^* (MPa)	0.16	160 .. 380	0.16	310 .. 750
a_{corr}	0.044 .. 0.063		0.033..0.046	

The lowest 'real' values of Y^* in Table 5.2 were used to calculate the charge transfer correction for the simulations, resulting in $a_{\mathrm{corr}} = 0.063$ for particle-particle contacts and $a_{\mathrm{corr}} = 0.046$ for particle-wall contacts. Charge transfer in both types of contact is further accelerated by an artificial acceleration factor $a = 15$, so that the charge transfer rate in the simulations are expected to be at least 15 times faster than in a real case with a given work function difference.

6. RESULTS AND DISCUSSION

To determine the magnitude of the charging in different conditions, several experiments were carried out in different humidities. Guided by preliminary simulations, simulations were run to produce saturation charges corresponding to the experimental results. Before studying the experimental and simulated results more closely, a general view of the similarities and differences between the simulated and experimental results are discussed.

6.1 General overview

In the case of uncharged particles, the qualitative behaviour of the simulated and experimental beds are fairly similar as illustrated in Figure 6.1. However, it is noticed that the height of the experimental bed is consistently lower than in the simulations with respective fluidization velocities. This difference can be explained by at least four reasons:

1. The correlation used for drag factor affects the bed height. For example the Di Felice correlation would produce lower bed heights than the Wen-Yu drag factor, as the drag factor corresponding to the fluidization velocities sued uin the experiments would be smaller.

2. The dimensions of the glass pipe are not accurate. An increase of 1 mm in either of the cross-sectional dimensions causes an 10% increase on the cross-sectional area and respective drop in the superficial velocity.

3. The pressure sensor operates on a dynamic principle, so a small flow is allowed trough the sensor. At the pressure range used in the experiments ($\sim$ 150 Pa), the relative drop of the superficial velocity is maximally about 2 %.

4. It is possible that there is minor gas leaks from the system after the flow controller but before the bed.

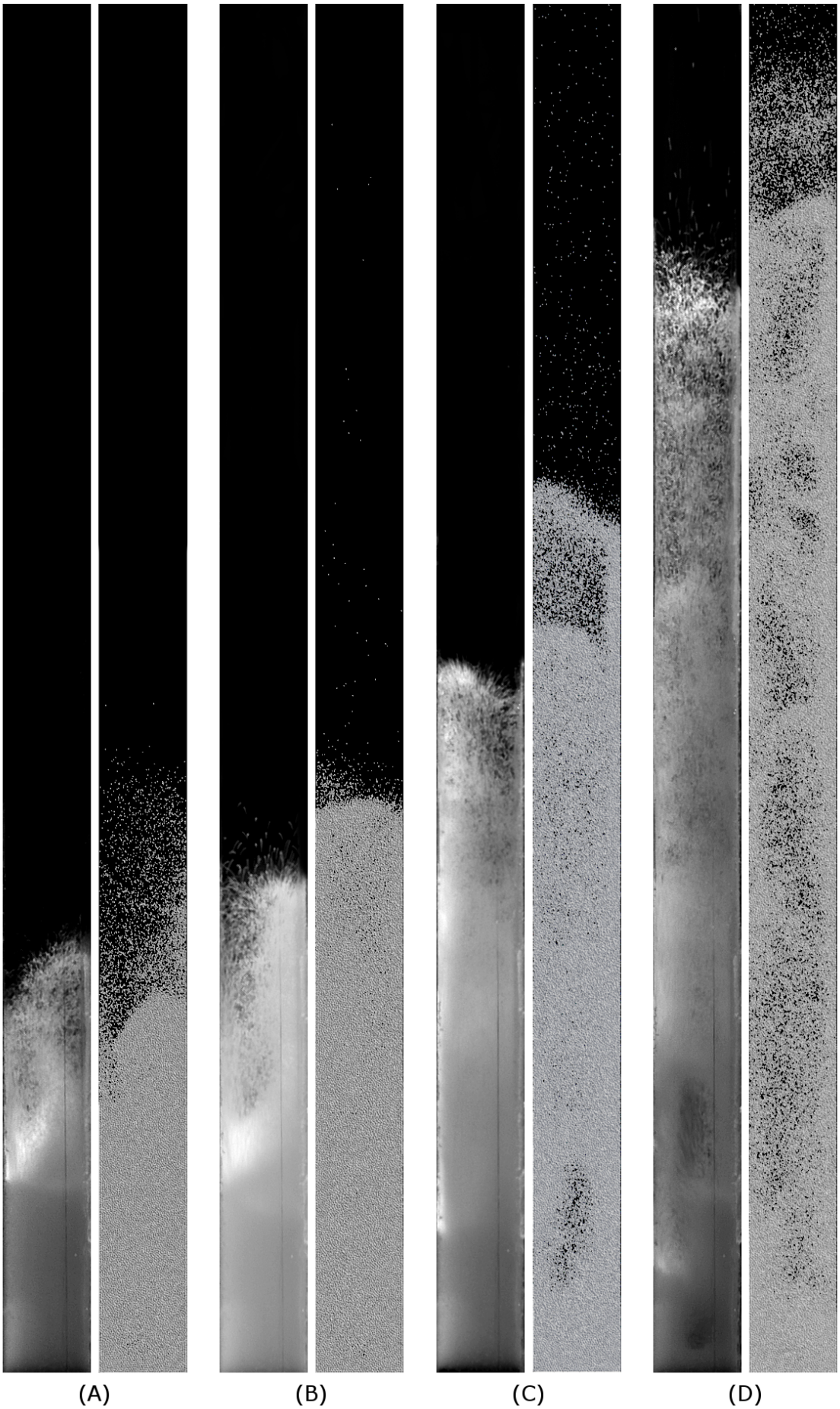

Figure 6.1 *Snapshots of the experimental (left) and the simulated bed (right) with different superficial velocities. Panel (A):* $U/U_t = 0.34$*, Panel (B):* $U/U_t = 0.51$*, Panel (C):* $U/U_t = 0.68$*, Panel (D):* $U/U_t = 0.85$*.*

All of the reasons above tend to render the experimental bed lower than the simulated bed. This affects triboelectric charging by decreasing the area available for particle-wall contacts and by altering the electric field: the lower the bed, the stronger electric field is incurred on the walls given a certain total charge. Thus it is expected that the simulations predict smaller saturation charges than if the bed height would more accurately match the height of the experimental bed.

However, the observed differences are not so substantial that they would prevent comparing the simulated and experimental results with respect to triboelectric charging. The pertinent question is how well the effects of triboelectric charging are captured by the model.

6.2 Charge of the particles

Several experiments were carried out in different relative humidities ranging from dry 0 % to 60 %. Besides final charge, pressure drop during the fluidization was measured. The duration of the experiments was set to 30 minutes, which was considered sufficient for the charge in the bed to saturate in most conditions.

Before pouring the particles into the bed, the humidity and the mass flow rate were allowed to settle to the desired values. The relative humidity was kept in the range of ± 1 % of the desired value in each experiment. The mass flow rate was set to 3 $\mathrm{l_n/min}$, corresponding to a superficial velocity of $U = 0.51U_t$. The mass of the particles was measured before each experiment and after measuring the final charge, being 1.5 ± 0.03 grams.

A fresh set of particles was deployed for each persistent measurement session, but the same set was used in successive experiments. The charge on the particles was erased between the experiments by briefly fluidizing them in a high relative humidity (> 60 %), so that the charge before the next experiment was between ± 3 nC/g.

The charge-to-mass ratios measured after fluidization are depicted in Figure 6.2. It is notable that the total charge in dry conditions is strictly positive, but the polarity changes at about 30 % relative humidity, being lowest at about 50 % RH. A similar result was obtained also with using higher fluidization velocities, and it strongly suggests that there is more than one charge transfer mechanisms present.

The significant variance of the charge-to-mass ratio in each humidity might be due

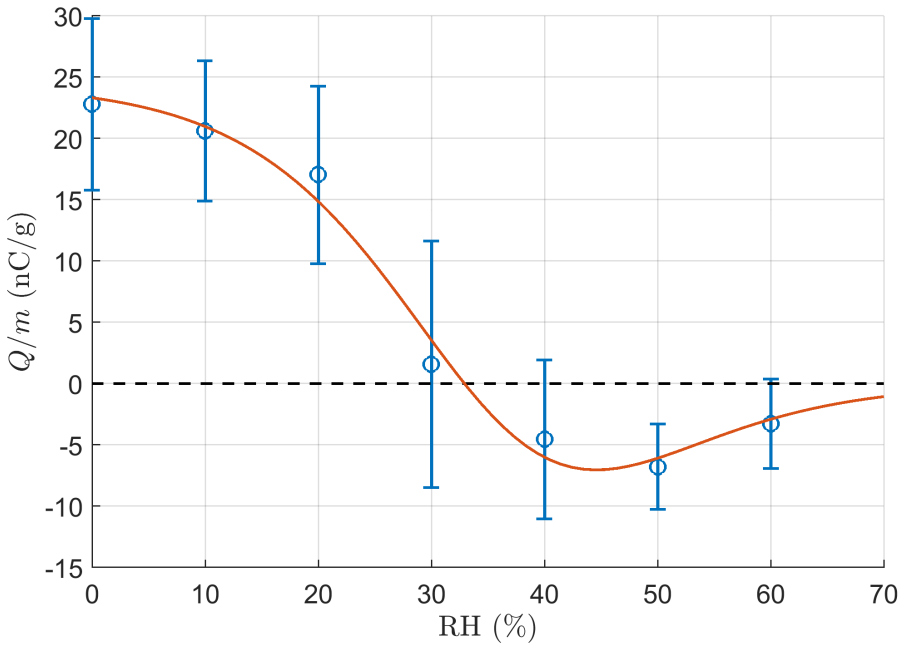

Figure 6.2 *Charge per mass measured in different conditions with using* $U = 0.51U_t$. *Error bars: 95 % confidence intervals.*

that although the total charge is initially nearly zero, there may be a considerable charge distribution among the particles, not to mention the charge distribution on the particle surfaces. In this sense, the history of the particles may have influence on the results.

It was also observed that the behaviour of the bed was very sensible to the relative humidity especially around 30 % RH; for example an 1% increase of relative humidity resulted in a visible change of the pressure loss and the height up to which particles were agglomerated on the wall.

However, there is notable variance even in condition where the dependency of the final charge on humidity is not so prominent (at 0..20% and 40..60% RH). Also, the variance is not notably lower if only the results obtained with using unused particles is considered. This makes to conclude that the inaccuracy in controlling the relative humidity and the reuse of the particles are not alone responsive for the variation in the results.

One candidate for explaining the variance of the charge-to-mass ratio is the condition of the glass surface: if the charge transfer is due to the ions originating from the glass

Table 6.1 *The the effective work function differences used in the preliminary simulations with corresponding values of e/g and equilibrium charges. The resulting charge-to-mass ratio from the simulations are given in the last column.*

e/g	$\frac{\Delta\varphi}{z_c e}$ (kV/m)	q_{eq} (pC)	$\lvert Q_\infty \rvert / m$ (nC/g)
0	0	0	0
2	± 627	± 1.34	8.2
4	± 886	± 1.89	13.1
8	± 1250	± 2.68	20.3

surface, the results may depend on the ability of the source of the charge carriers to replenish between the measurements. The effects of possible depletion of charge could be reduced by running humid gas trough the empty bed for a longer time between the experiments.

In order to reasonably compare simulated and experimental results, simulations need to produce saturation charges corresponding to experimentally results. To examine the dependency of the total charge on the effective work function difference, preliminary simulations were run using effective work function differences given in Table 6.1. The effective work function differences were selected according to the values of e/g given in Table 6.1, which were chosen large enough to presumably have a visible effect on the fluidization behaviour.

Corresponding to each non-zero value of e/g in Table 6.1, two simulations were run: one with a positive work function difference and one with a negative work function difference. As expected, opposite work function differences produce a similar charge-to-mass ratio but an opposite charge polarity, as seen in Figure 6.3.

It was found that Equation 3.12 corresponds the time evolution of the total charge fairly well, as indicated by the fitted curves in Figure 6.3. For comparability with the measurements, the total charge was scaled by the mass of the particles.

Equation 3.12 was fit simultaneously to each pair of simulation results corresponding to each value of e/g given in Table 6.1. This gives the absolute values of the saturated charge-to-mass ratios corresponding to each value of e/g.

The saturation charges obtained from the preliminary simulations cover very well the range of the experimental results, as seen when comparing simulated charge-to-mass

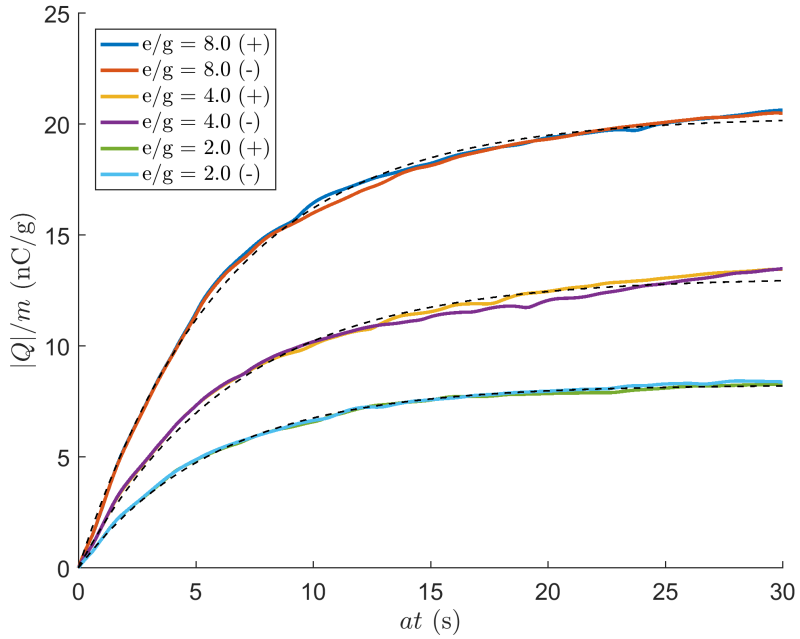

Figure 6.3 *Charge-to-mass ratio as a function of time. The simulation time t is scaled by the acceleration factor a. The sign of the effective work function difference used in each simulation is indicated by '+' or '-' in the legend. The dashed lines represent Equation 3.12 fitted to the simulated result using the least-squares method.*

ratios given in Table 6.1 and the experimental results shown in Figure 6.2. It was also found that the saturation charge is almost directly proportional to the effective work function difference. By linearly interpolating the charge-to-mass ratios given in Table 6.1 to the experimental charge-to-mass ratios, one obtains an estimate for the effective work function difference producing the desired charge-to-mass ratio. Such interpolated values for the effective work function differences corresponding to the experimental charge-to-mass ratios are shown in 6.2.

By running simulations with using effective work function differences given in Table 6.2, charge-to-mass ratios very close to the experimental ones are obtained, as shown in Figure 6.4. The results of these simulations should match with the experimental results in different conditions as close as possible in limits of accuracy of the simulations and the validity of the underlying mathematical models.

The correspondence of the experimental and simulated charge-to-mass ratios does not tell much about the validity of the charge transfer model. Actually, any model which would product a reasonable saturation charge would succeed, as the model

Table 6.2 *The mean values of the charge-to-mass ratios in different humidities and the corresponding effective work function differences.*

RH (%)	Q/m (nC/g)	$\frac{\Delta\varphi}{z_c e}$ (kV/m)
0	22.8	736
10	20.6	706
20	17.0	653
30	1.58	217
40	-4.53	-368
50	-6.78	-450
60	-3.26	-312

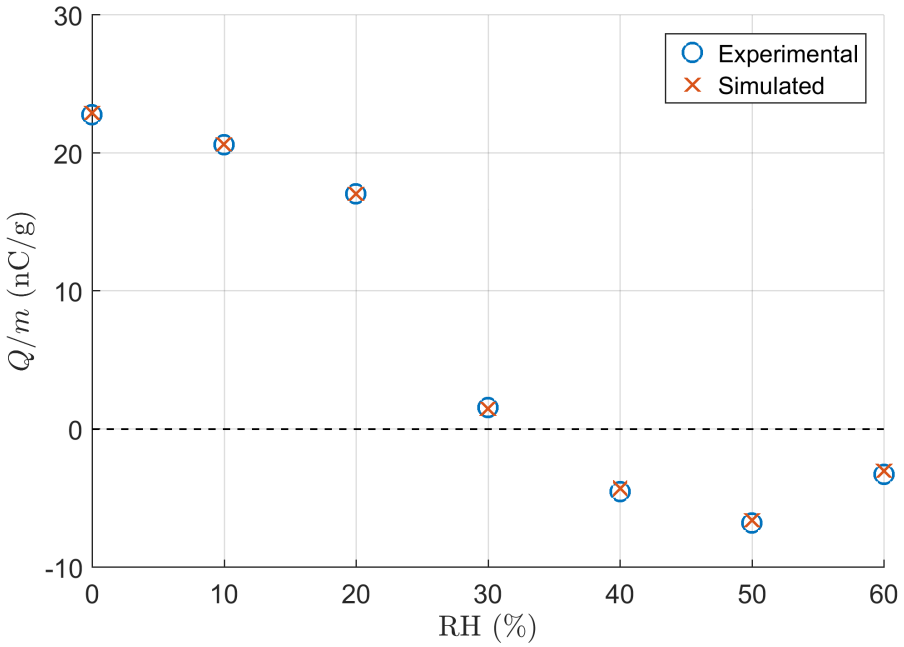

Figure 6.4 *The mean values of the measured charge-to-mass ratios in different humidity conditions with the corresponding simulation results.*

parameters (here the effective work function difference) can always be adjusted to produce a desired total charge. For validity purposes, the model should be tested in such conditions that the effective work function difference is not expected to vary (eg. in a certain humidity and temperature), but the total charge is changed by altering the other conditions in the bed.

To briefly study the dependency of the total charge on the fluidization velocity, additional simulations were run in with using $U/U_t = 0.68$ and $U/U_t = 0.85$, us-

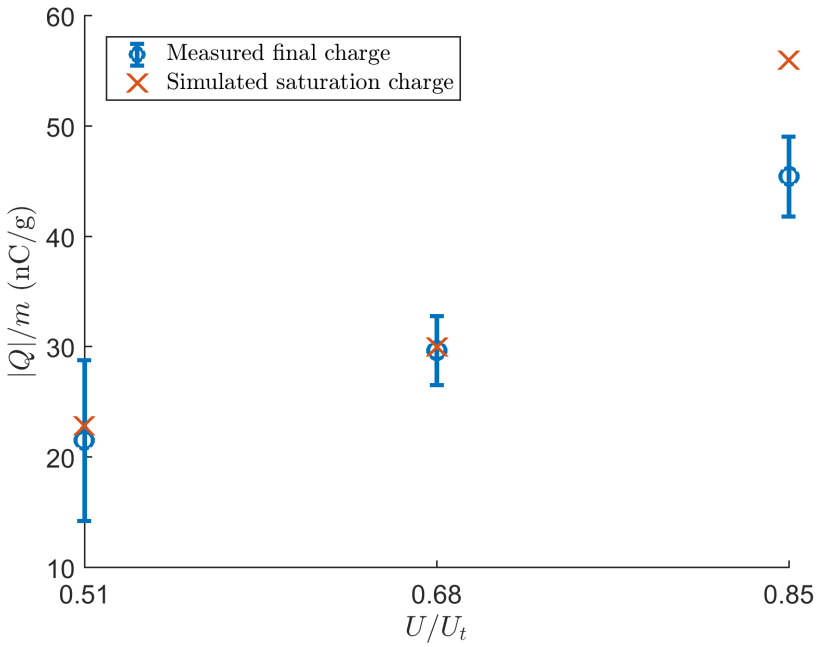

Figure 6.5 *The measured final charge and the simulated saturation charge in different fluidization velocities. Error bars: 95 % confidence intervals of the measured charge.*

ing the effective work function difference corresponding to 0 % RH. The resulting charge-to-mass ratios are plotted in Figure 6.5 along with corresponding experimental charge-to-mass ratios. It is found that the results match very well in lower velocities. At the highest fluidization velocity the simulated result diverges from the experimental results, which is at least partially accounted to the differences in bed height discussed before.

The correspondence of the measured and simulated results seen in Figure 6.5 is somewhat promising. Still this can be just a coincidence: the effective work function differences used in the simulations would probably yield different saturation charges if the behaviour of the experimental bed was better captured by the simulation model.

6.2.1 Particle agglomeration

It is suspected that particles agglomerated on walls may significantly affect the saturation charge, as an adhered layer of particles effectively prevents further particle-wall contacts. As illustrated in Figures 6.7 and 6.10, a thick, stationary layer of

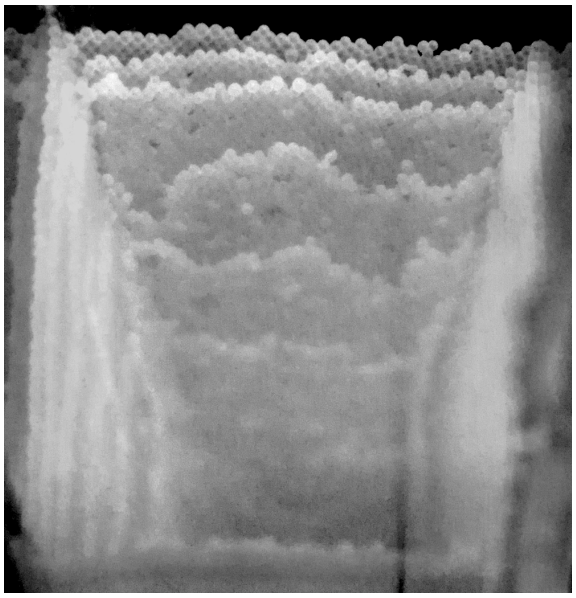

Figure 6.6 *Particles adhered on the wall after fluidization in 0 % RH.*

particles accumulates on the wall in the experiments. In conditions where triboelectric charging is strong enough, one can follow with the bare eye how the layer of particles gradually builds up on the wall. Typically, multiple layers of particles agglomerate on each other as seen in Figure 6.6.

Adhering of particles is also observed in the simulations as seen in Figure 6.8, but the results distinctly differ from the experiments: In the simulations, particles adhere to much greater heights than in the experiments. Moreover, only one layer of particles is adhered instead of agglomeration multiple layers. As the mass adhered to the walls in simulations is relatively small, the resulting change in dynamics of the bed are minor when compared to the experiments.

In the simulations the adhering affects for example the vertical velocity profile of the particles as shown in Figure 6.9: the average vertical velocity of the particles next to the wall is virtually zero in a simulation corresponding to 0 % RH. In the case of 30 % RH the effective work function is small and the velocity profile shows only a minor deviation from an uncharged case.

To quantitatively depict the build-up of the stationary wall layer, root-mean-square speed of the particles on the wall was considered in terms of PIV. Although PIV does not account for the movement of individual particles but rather the average motion at certain parts of the imaged area, it is used for comparing the velocity of

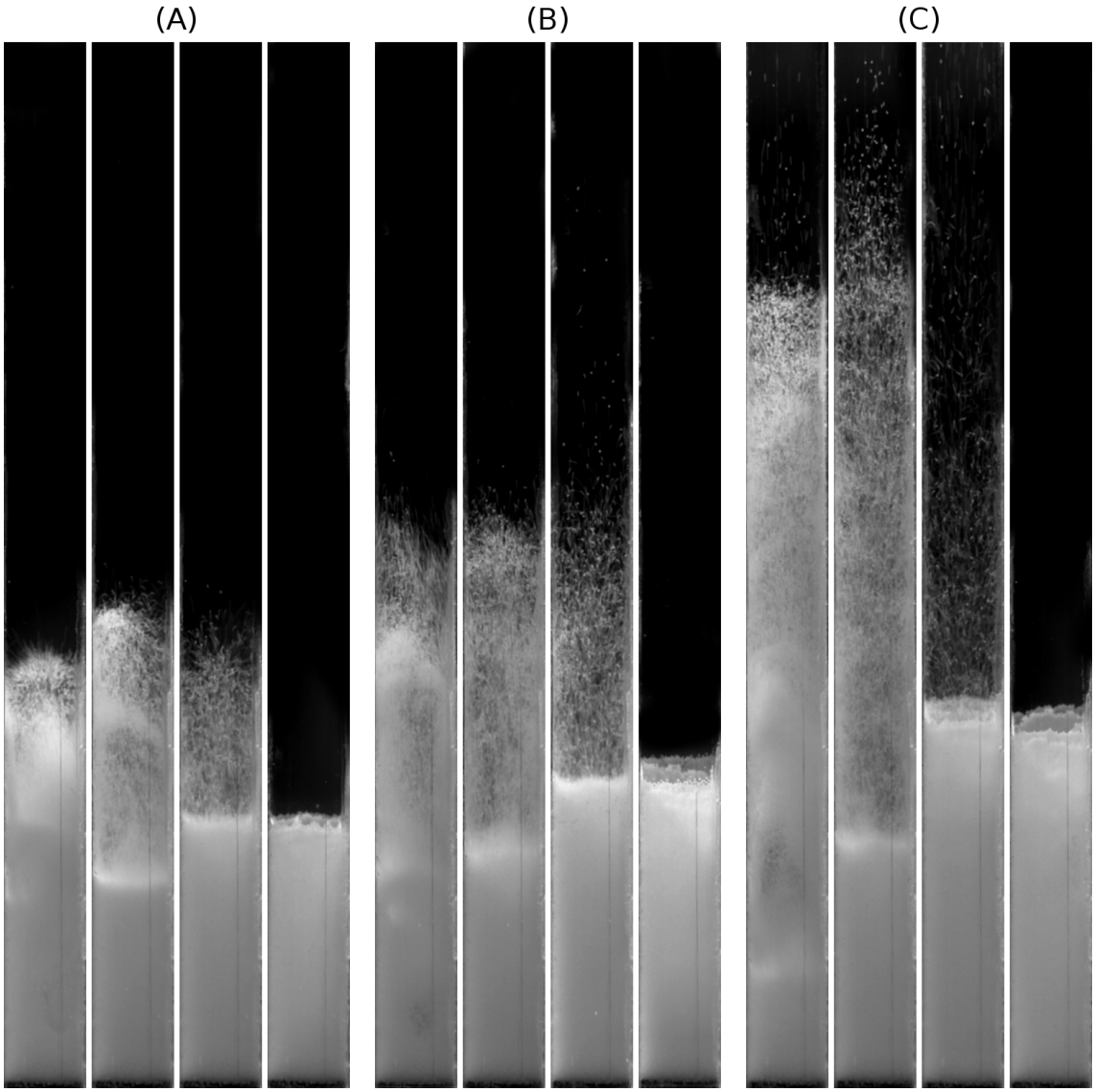

Figure 6.7 *Snapshots of the experimental bed (from left to right) at 0, 3 and 15 minutes from the beginning of the fluidization and and after the fluidization (right) in 0 % RH. Panel (A):* $U/U_t = 0.51$*, Panel (B):* $U/U_t = 0.68$*, Panel (C):* $U/U_t = 0.85$*.*

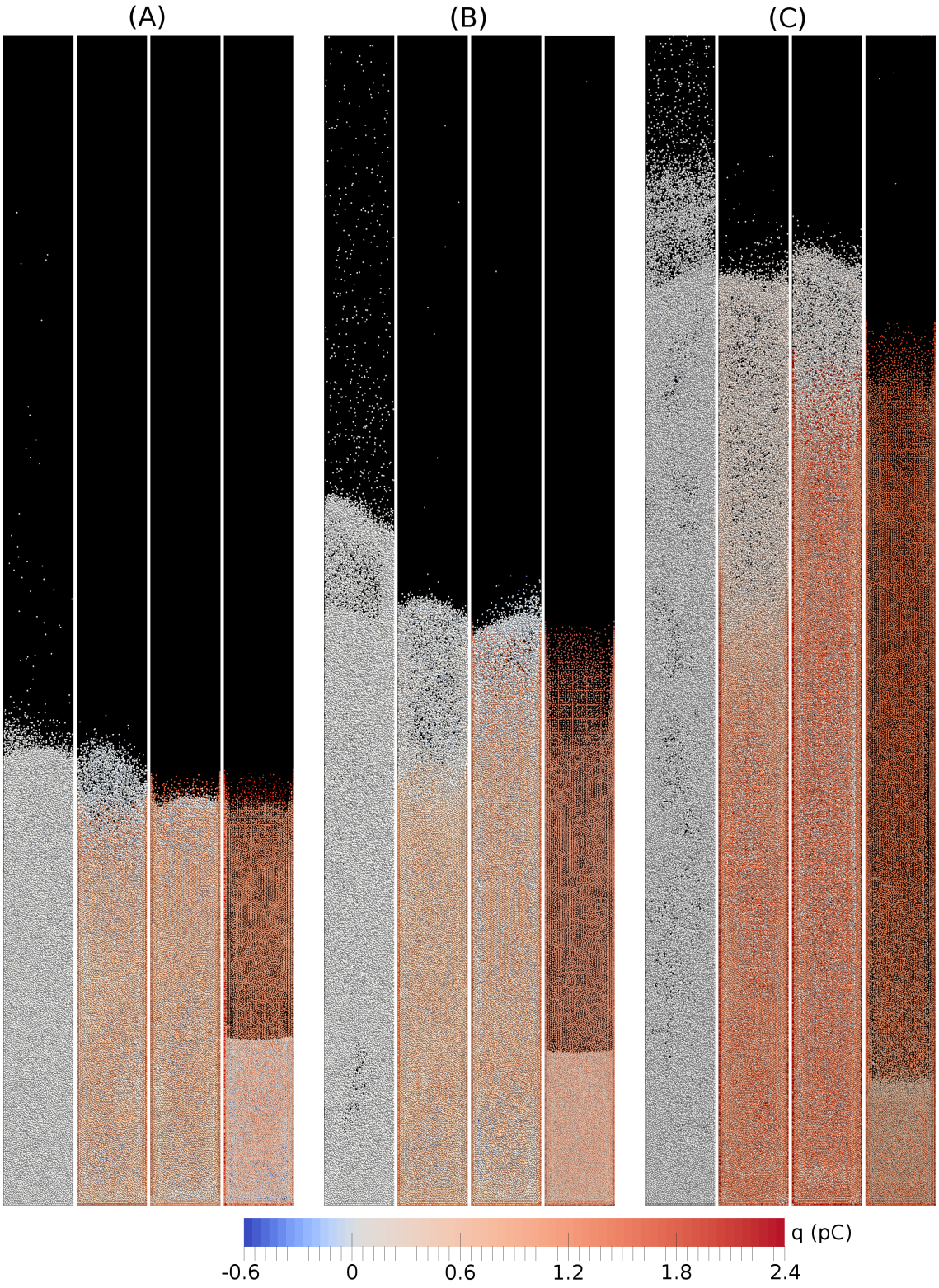

Figure 6.8 *Snapshots of the simulated bed (from left to right) at 0, 15 and 30 seconds of deaccelerated simulation time and after the fluidization in a simulation corresponding to 0 % RH. The particles are colored according to their charge to emphasize the particles adhered to the wall. Panel (A):* $U/U_t = 0.51$*, Panel (B):* $U/U_t = 0.68$*, Panel (C):* $U/U_t = 0.85$*.*

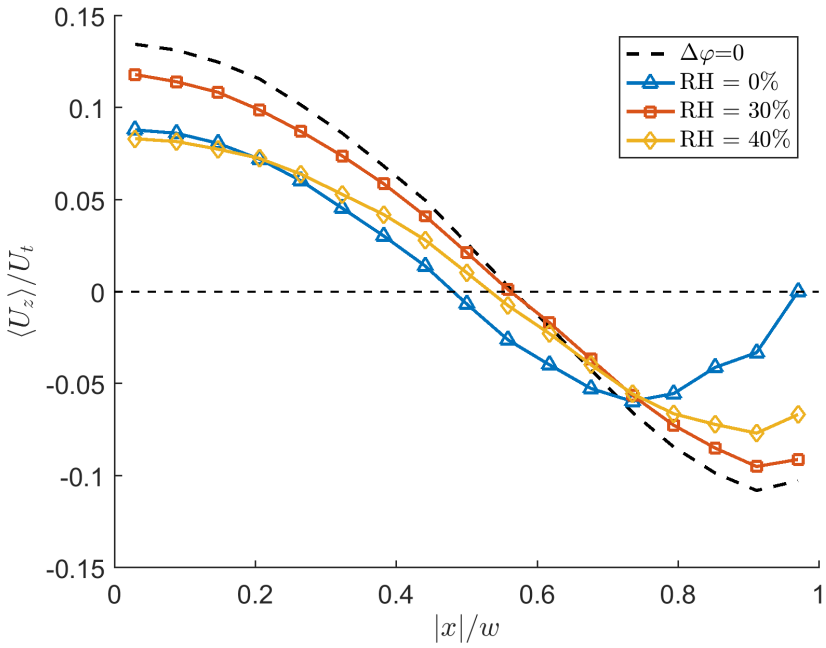

Figure 6.9 *Vertical velocity profile of the particles at pseudo steady state (*1.5..2.0 s*) in simulations corresponding to 0, 30 and 40 % RH. The dashed curve is the velocity profile of an uncharged case. w is the half-width of the bed.*

the wall layer between the simulations and the experiments.

As seen in Figure 6.11, the rms speed of the particles eventually approaches zero in all conditions considered expect in 30 % RH. This is due to a stationary layer of particles gradually growing up and covering the image area. In in 0 % and 20 % RH, it took a couple of minutes until the whole image area (up to a height of 30 mm from the bed inlet) was covered. In 30 % RH, a particle layer did not build up even after 15 minutes fluidization and the experiment was stopped.

In simulations, the root-mean-square speed of the particles in cases corresponding to experiments is like shown Figure 6.12. It is seen that in simulations corresponding to 0 % and 20 % RH, the speed reduces to near zero almost immediately, while in case of 30 % and 40 % RH the speed fluctuates around the initial value. The magnitude of the rms-speed is generally slightly lower than in the experimental bed.

As mentioned before, the particles form only one highly charged layer on the wall. The motion of the layer is not ceased completely, but the particles fluctuate around during the fluidization: this is also indicated by the residual rms-speed seen in Figure 6.12. Unlike in the experiments, the particle layer is not gradually building from the

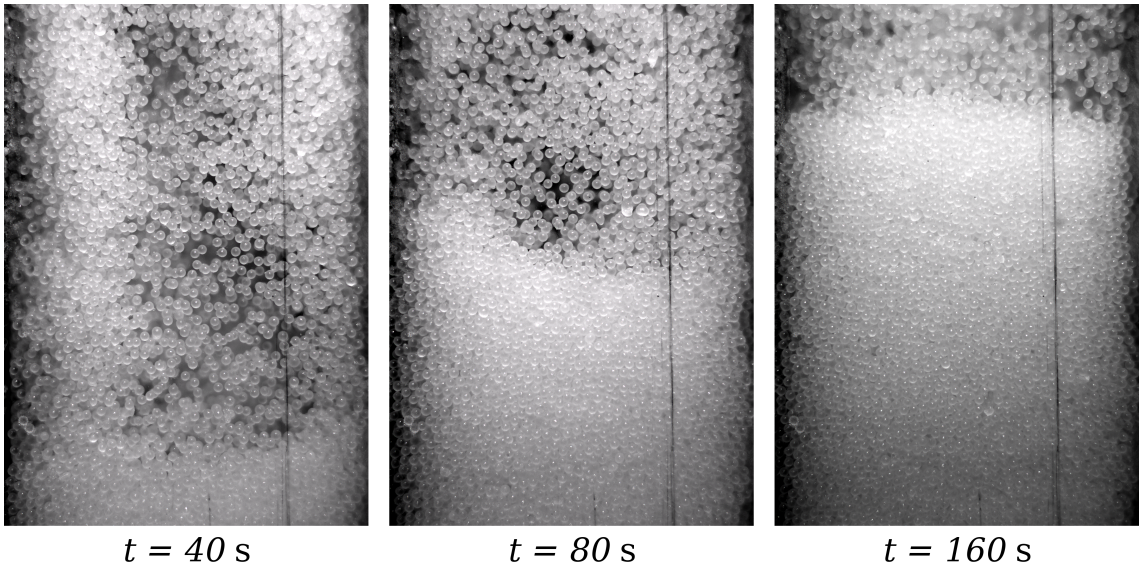

Figure 6.10 *Snapshots of the development of the wall layer at* $RH = 0$.

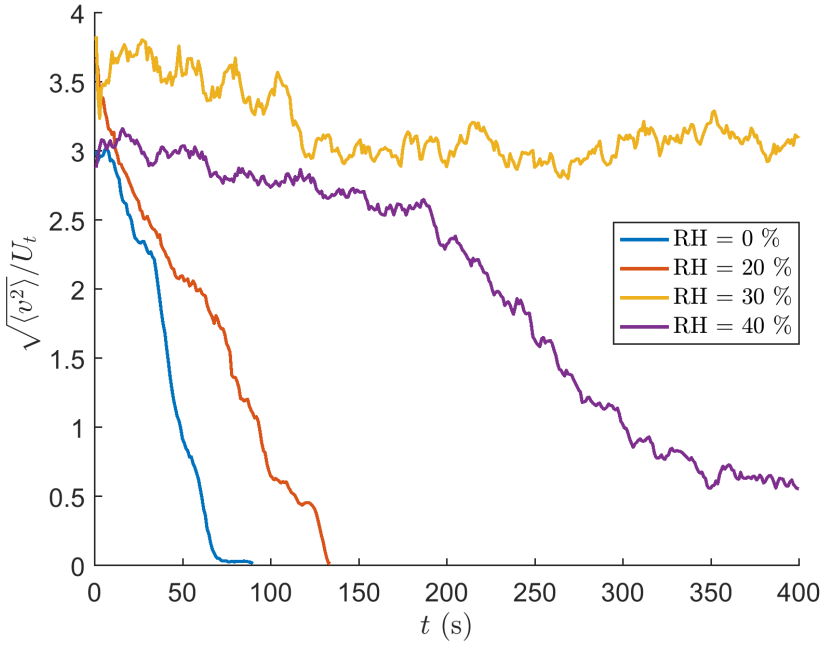

Figure 6.11 *The root mean square velocity of the particles on wall in experiments. For a cleaner picture, a moving average with a window size of* $t = 10$ s *is plotted instead of the actual velocity.*

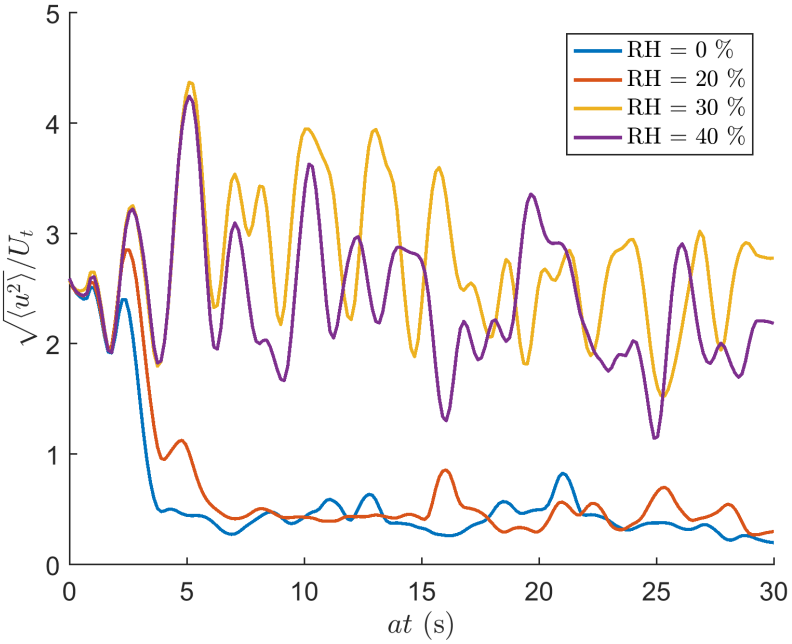

Figure 6.12 *The root mean square velocity of the particles on the wall in simulations. For cleaness, a moving average with a window size of* $at = 1.5$ s *is plotted instead of the actual velocity.*

bottom up. Instead, favourably charged particles are attracted and subsequently captured to the wall over the whole height of the bed. This explains the adhering of particles to greater heights in simulations than in experiments.

The fact that the motion of the particles on the wall does not completely cease in the simulations is due to the strong charges of the particles. The electrostatic forces between particles on the wall are repulsive and parallel to the wall. In the simulation corresponding to 0 % RH, for example, the charge of the particles on the wall is about 2 pC. For two averagely sized particles in contact, this results in a repulsive force about four times stronger than the gravitational force: it is clear that in lack of cohesive forces, the particles are unable to rest close to each other.

In addition to cohesive forces, the tendency of the particles to adhere on each other could be explained by a suitable arrangement of positively and negatively charged particles. Particles of both polarities are indeed present bed as seen in (Figure 6.13).

A bimodal particle charge distribution is developed in the bed if the effective work function difference is strong enough. This is the case for example in the simulation corresponding to 0 % RH as shown Figure 6.15. Generally, the particles on the wall

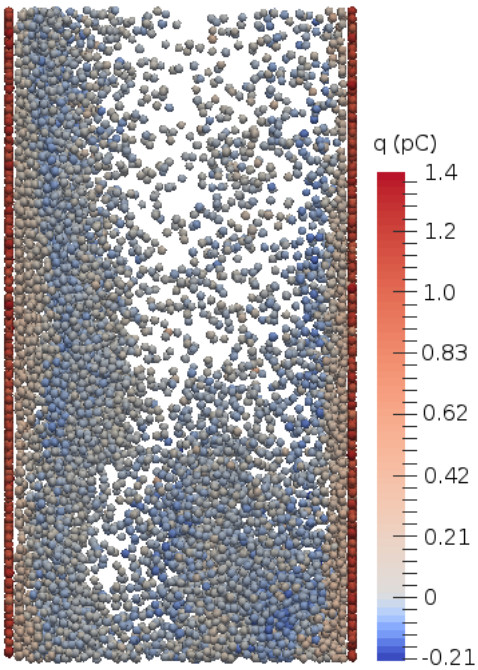

Figure 6.13 *A snapshot from the central part of the bed showing the charge of the particles in a simulation corresponding to 0 % RH.*

acquire strong charge as illustrated in Figures 6.13 and 6.14, while the charge of the other particles is near zero. In cases with a relatively low effective work function difference the charge distribution is unimodal, like in the case corresponding to 40 % RH.

It is possible that computational artefacts prevent particles from adhering to each other in the simulations, which would explain the discrepancy between simulated and experimental results. This point is further discussed is Appendix A.

However, it seems that if the acceleration factor is decreased, the gap between the peaks of the charge distribution decreases: it is possible that artificially increased charge transfer rate is responsible for the bimodal charge distribution observed in the simulations. The effect of the acceleration factor on the charge distribution is further discussed in Appendix B.

6.3 Pressure loss

Due to agglomeration of particles on the walls, the fluidized mass decreases and so does the pressure drop. In dry conditions, the charge transfer rate is rapid and the

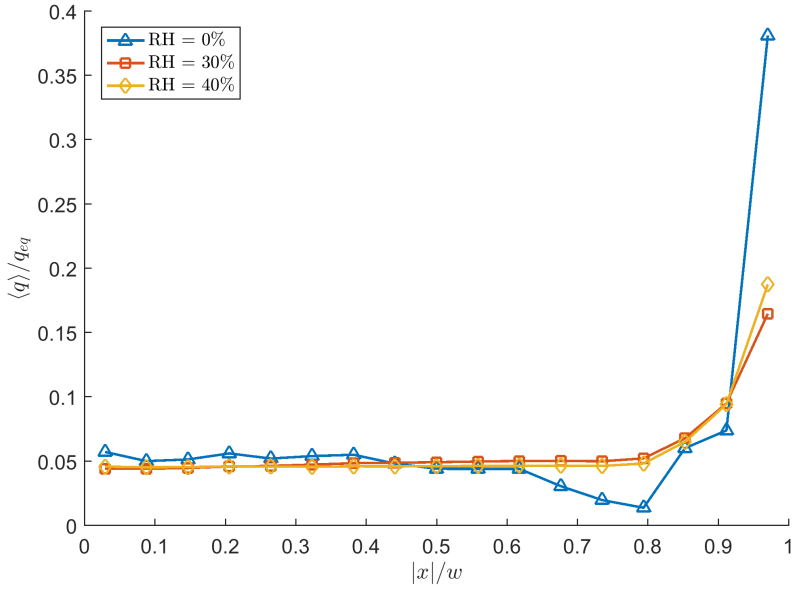

Figure 6.14 *Horizontal profile of the time-averaged particle charge at* 1.5..2.0 s *in simulations corresponding to 0 %, 30 % and 40 % RH. w is the half-width of the bed.*

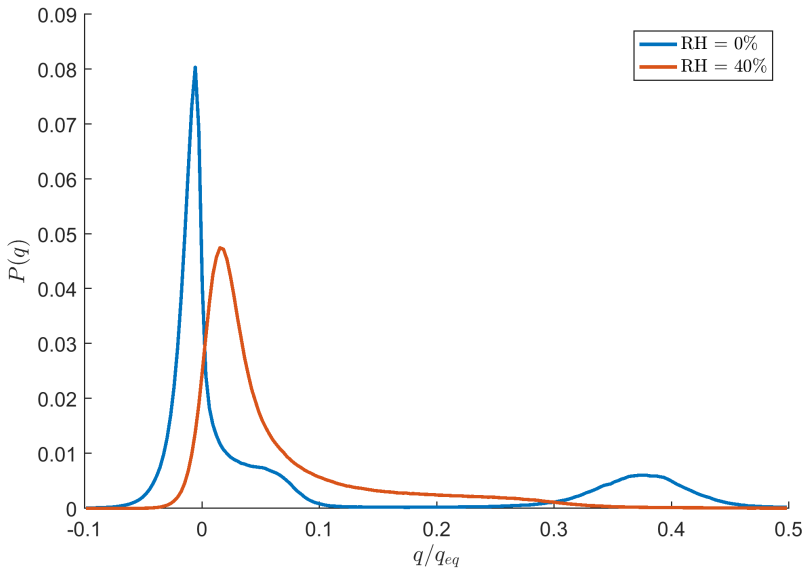

Figure 6.15 *Probability density function of the particle charge at the pseudo steady state ($t =$ 1.0..1.5s) in simulated cases corresponding to 0 % and 40 % RH .*

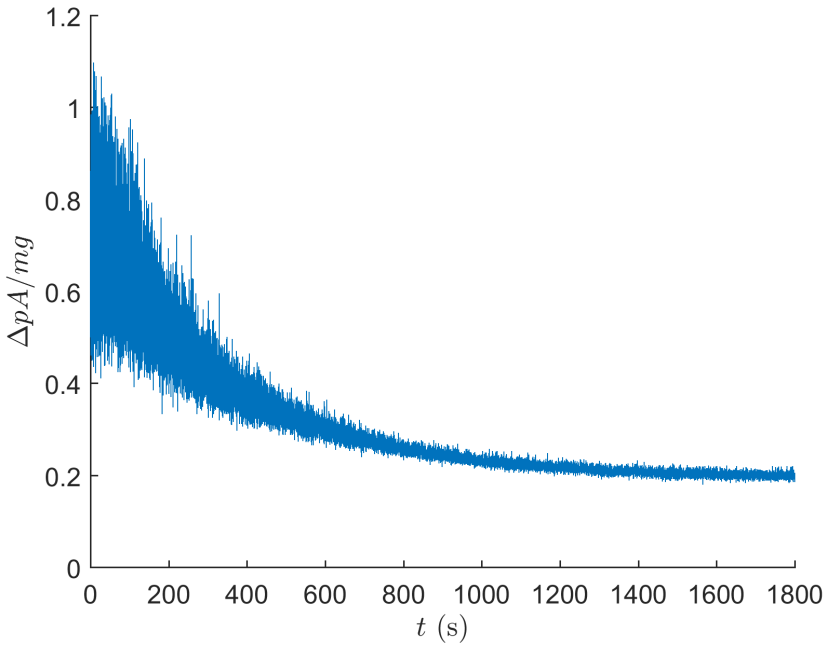

Figure 6.16 *Pressure loss at $RH = 0\%$ scaled by the weight of the particles (mg) and the cross-sectional area of the bed (A).*

effects on the pressure drop are clear. A representative result in Figure 6.16 shows how the pressure drop over the bed decreases over time. Subsequently, the volume fraction of the particles in the core region decreases and the slugging behaviour of the bed vanishes.

A correlation between the final total charge and the decrease of the pressure drop is illustrated in Figure 6.17. Pressure drop over the fluidizing device without particles is subtracted from the measured pressure difference to approximately obtain the pressure loss due to the particles only.

The fitted curve in Figure 6.17 is of form

$$\frac{\Delta p_i - \Delta p_f}{\Delta p_i} = 1 - \exp\left(-\frac{k}{m}\left(|Q| - |Q|_0\right)\right), \tag{6.1}$$

which is reasoned by the fact that the decrease of the pressure loss cannot exceed the initial pressure. $|Q|_0$ is the expected magnitude of charge where the agglomeration to the walls begins to take effect (at this charge, electrostatic forces are strong enough to induce adhering).

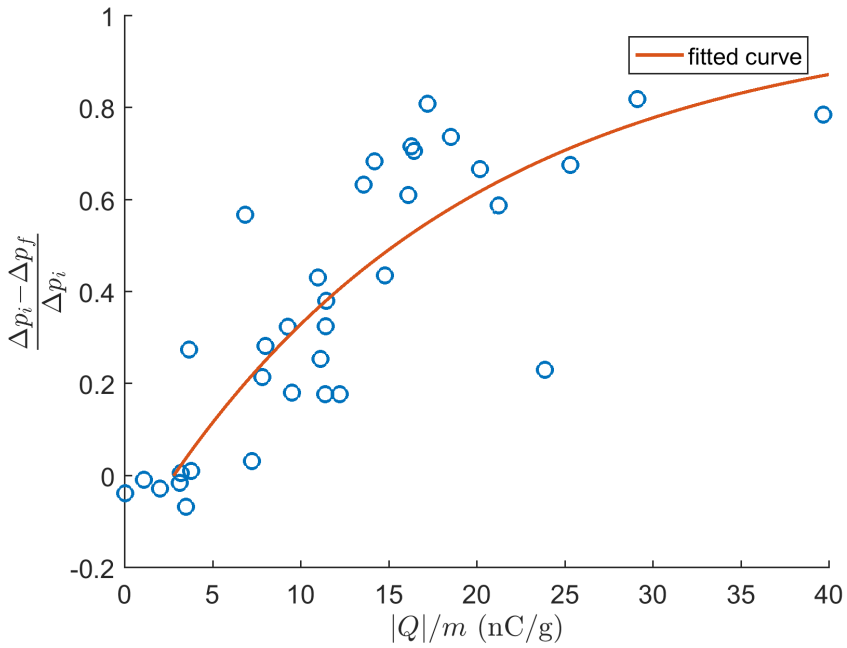

Figure 6.17 *The relation of the measured charge-to-mass ratio to the decrease in the pressure drop. The blue The initial and final pressure losses Δp_i and Δp_f are calculated as the mean value of the first and last 10 seconds of fluidization, respectively.*

In most measurements in 50..60 % RH or in 30 % RH , the pressure drop did not decrease virtually at all during fluidization. Occasionally, the pressure drop began to decrease only after a fluidization of several minutes, indicating that not enough charge was accumulated until that point. A couple of times the mass of the particles was significantly greater after the fluidization than before, indicating that the particles were wetted. In these cases, the charge accumulated was virtually zero.

The pressure drop in the simulations is not as prominent as in the experiments as depicted by Figure 6.18. This is accounted to the fact that in simulations the mass adhered to the walls is relatively small, resulting in a minor decrease in fluidized mass when compared to the experiments.

All in all, the most notable side-effect of triboelectric charging, namely the adhering to the walls is qualitatively captured by simulations. Unfortunately, the simulations do not explain agglomeration of multiple layers of particles to the walls. This renders it difficult to compare any aspect between the simulations and the experiments despite the total charge.

This does not necessarily mean that the charging model is invalid, but the effective

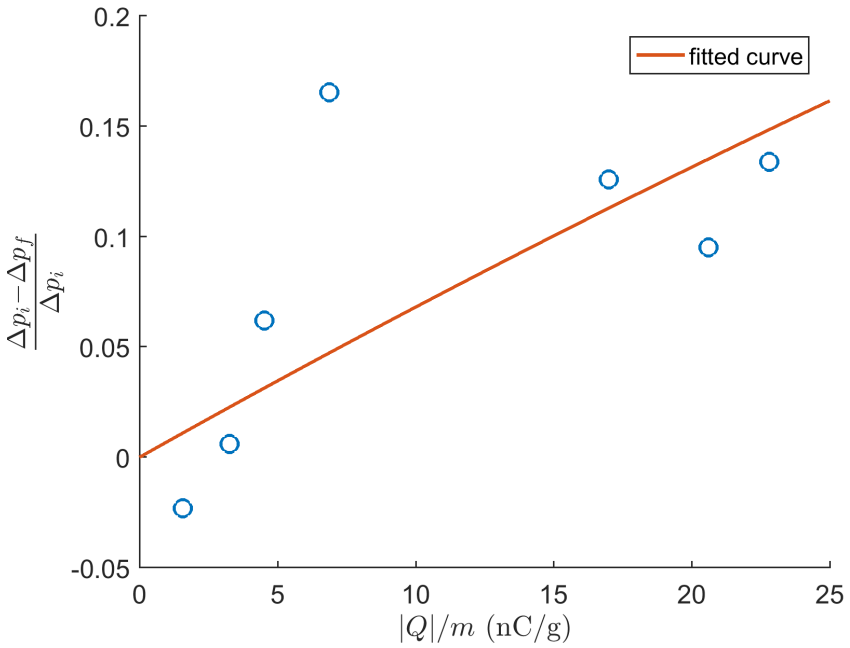

Figure 6.18 *The relation of the final charge-to-mass ratio to the decrease in the pressure drop in simulations. The initial and final pressure losses Δp_i and Δp_f are calculated as the mean value of the first and last 0.2 seconds of the simulation, respectively.*

work function differences deduced in this work would most probably produce different saturation charges if the behaviour of the simulated bed would more closely represent the behaviour of the experimental bed.

6.4 Nature of the transferred charge

As discussed in Chapter 3, the factors affecting to the net charge transfer between two surfaces are numerous. Here a rough explanation is proposed for explaining the experimentally observed charge-to-mass ratios.

As seen in Figure 6.2, the charge-to-mass ratio is positive in dry conditions (0..20 % RH). In terms of electron transfer, this could be addressed to electrons donored from polyethylene to the surface of the glass. However, it is proposed that the positive charge on the particles could be due to the same actor which generally makes surfaces of glass negatively charged in aqueous solutions [56, 57], namely the silanol groups on the glass surface.

It is supposed that weakly bonded protons of the silanol groups accommodate them-

selves on the polyethylene surfaces, probably forming covalent bonds with the anionic heads of scissioned polymer chains of polyethylene. The observed change of polarity around 30 % RH in turn is accounted to negatively charged hydroxide, which preferably adheres on the hydrophobic polyethylene surfaces. In even higher humidities, the charge is eventually dissipated due to ioinic conductivity, driving the charge-to-mass ratio towards zero.

7. CONCLUSIONS

A simple triboelectric charging model based on effective work function difference between fluidized particles and the bed walls was applied to simulate the behaviour of an experimental fluidized bed. It was found that the simulations capture partially the most discernible side-effect of static electricity in the bed, as a layer of highly charged particles accumulate on the wall.

It was also provided that it is straightforward to adjust the effective work function difference to force the final charge of the experiments and simulations to match. Unfortunately, the effects of triboelectric charging are not completely captured in the simulations.

The most notable difference between simulated and experimental results is that in favourable conditions, multiple layers of particles agglomerate to the walls of the experimental bed. In simulations in turn, only a monolayer of strongly charged particles is adhered. This inconsistency renders it problematic to compare the simulated bed to the experimental one and should be addressed for further improving the model.

Basing only on the results of this work, it is hard to state if the total charge accumulated on the particles is ultimately limited by the electric field or the depletion of charge carriers. It is apparent that verifying the triboelectric charging model requires studying more closely experimental cases where the environmental conditions such as humidity and temperature are kept constant.

The validity of the mtriboelectric charging odel would be strongly supported if a certain effective work function difference would correctly predict triboelectric charging in several different cases, in which for example the geometry of the bed and the mass of the particles are varied. As fluidization alone brings a fair amount of uncertainty and inaccuracy to the results, experiments should preferably be conducted in more simple experimental setups such as a vibrated bed.

Introducing an external electric field to the interface of particles and the wall would enlighten the role of electric field in the charge transfer. According to Equation 3.8, the charge accumulated on a particle should be linearly dependent of the electric field at the contact point. An external electric field could also help to reveal if the saturation charge is limited by other factors than just the electric field in the contact point. Also, impact charging experiments similar to the ones conducted by Matsusyama and Yamamoto [30] could be useful to judge the validity of the charging model in a single particle-wall contact.

It is reasonable to state that the model is not necessarily mature enough to be verified through fluidization experiments. The model should be more thoroughly tested against less complicated experimental cases: only when the fundamentals are valid, the model can be reasonably applied to larger systems.

A step down in complexity would be to apply the present model in a vibrated bed. This kind of experiment has already been conducted in cooperation with Kolehmainen *et al.* in an unpublished study [58]. The goal is that the effective work function differences obtained from a simple experiment would correctly predict triboelectric charging in a fluidized bed or in any other device involving gas-particle flow.

BIBLIOGRAPHY

[1] S. Matsusaka, H. Maruyama, T. Matsuyama, and M. Ghadiri, "Triboelectric charging of powders: A review," *Chemical Engineering Science*, vol. 65, no. 22, pp. 5781–5807, 2010. [Online]. Available: http://www.sciencedirect.com/science/article/pii/S0009250910004239

[2] Z. L. Wang, "Triboelectric nanogenerators as new energy technology and self-powered sensors - Principles{,} problems and perspectives," *Faraday Discuss.*, vol. 176, no. 0, pp. 447–458, 2014. [Online]. Available: http://dx.doi.org/10.1039/C4FD00159A

[3] L. S. McCarty and G. M. Whitesides, "Electrostatic charging due to separation of ions at interfaces: contact electrification of ionic electrets," *Angewandte Chemie International Edition*, vol. 47, no. 12, pp. 2188–2207, 2008.

[4] D. J. Lacks and R. M. Sankaran, "Contact electrification of insulating materials," *Journal of Physics D: Applied Physics*, vol. 44, no. 45, p. 453001, 2011.

[5] B. A. Kwetkus, "Particle triboelectrification and its use in the electrostatic separation process," *Particulate Science and Technology*, no. 1, pp. 55–68.

[6] A. G. Bailey, "Electrostatic phenomena during powder handling," *Powder Technology*, vol. 37, no. 1, pp. 71–85, 1984. [Online]. Available: http://www.sciencedirect.com/science/article/pii/0032591084800078

[7] J. Cross, *Electrostatics: Principles, problems and applications*. Bristol: Adam Hilger, 1987.

[8] A. H. Chen, H. T. Bi, and J. R. Grace, "Measurement of particle charge-to-mass ratios in a gas–solids fluidized bed by a collision probe," *Powder Technology*, vol. 135–136, pp. 181–191, 2003. [Online]. Available: http://www.sciencedirect.com/science/article/pii/S0032591003001967

[9] G. Falkovich, *Fluid mechanics: A short course for physicists*. Cambridge University Press, 2011.

[10] P. N. Chandramouli, *Continuum Mechanics*. Yes Dee Publishing Pvt Ltd., 2014.

[11] M. L. Moukalled F. and D. M., *The Finite Volume Method in Computational Fluid Dynamics*. Springer, 2015.

[12] L. Leal, *Advanced transport phenomena: fluid mechanics and convective transport processes*. Cambridge University Press, 2007.

[13] Y. T. C. Crowe, M. Sommerfeld, *Multiphase Flows With Droplets And Particles*. CRC Press, 1998.

[14] C. J. Greenshields, *OpenFOAM Programmer's Guide*, OpenFOAM Foundation Ltd.

[15] J. Kolehmainen, A. Ozel, and S. Sundaresan, "A hybrid approach to computing electrostatic forces in fluidized beds of charged particles," *AIChE Journal*, vol. 39, no. 7, April 2016.

[16] P. Cundall and O. Strack, "A discrete numerical model for granular assemblies," *Geotechnique*, vol. 29, 1979.

[17] Y. Tsuji, T. Tanaka, and T. Ishida, "Lagrangian numerical simulationof plug flow of cohesionless particles in a horizontal pipe," *Powder Technology*, vol. 71, no. 239-250, 1992.

[18] D. Antypov and J. Elliott, "On an analytical solution for the damped hertzian spring," *EPL (Europhysics Letters)*, vol. 94, no. 5, p. 50004, 2011.

[19] K. Jari, A. Ozel, C. Boyce, and S. Sundaresan, "Triboelectric charging of monodisperse particles in fluidized beds," *AIChE Journal*, vol. 39, no. 7, August 2016.

[20] L. Schiller and A. Naumann, "Uber die grundlegenden berechnungen bei der schwekraftaubereitung," *Zeitschrift des Vereines Deutscher Ingenieure*, vol. 77, no. 12, pp. 318–320, 1933.

[21] Y. Y. Wen C.Y., "Mechanics of fluidization," *Chem. Engr. Prog. Sump. Series*, vol. 62, p. 100, 1966.

[22] R. Di Felice, "The voidage function for fluid-particle interaction systems," *International Journal of Multiphase Flow*, vol. 20, no. 1, pp. 153–159, 1994.

[23] S. R. Subramanian, "Flow through Packed and Fluidized Beds."

[24] G. Hendrickson, "Electrostatics and gas phase fluidized bed polymerization reactor wall sheeting," *Chemical Engineering Science*, vol. 61, no. 4, pp. 1041–1064, 2006. [Online]. Available: http://www.sciencedirect.com/science/article/pii/S0009250905006433

[25] W. R. Harper, *Contact and frictional electrification.* Laplacian Press Morgan Hill, CA, 1998.

[26] J. Lowell and A. C. Rose-Innes, "Contact electrification," *Advances in Physics*, vol. 29, no. 6, pp. 947–1023, 1980. [Online]. Available: http://dx.doi.org/10.1080/00018738000101466

[27] D. K. Davies, "Charge generation on dielectric surfaces," *Journal of Physics D: Applied Physics*, vol. 2, no. 11, p. 1533, 1969. [Online]. Available: http://stacks.iop.org/0022-3727/2/i=11/a=307

[28] A. R. Akande and J. Lowell, "Charge transfer in metal/polymer contacts," *Journal of Physics D: Applied Physics*, vol. 20, no. 5, p. 565, 1987. [Online]. Available: http://stacks.iop.org/0022-3727/20/i=5/a=002

[29] J. Lowell, "Contact electrification of silica and soda glass," *Journal of Physics D: Applied Physics*, vol. 23, no. 8, p. 1082, 1990. [Online]. Available: http://stacks.iop.org/0022-3727/23/i=8/a=014

[30] T. Matsusyama and H. Yamamoto, "Impact charging of particulate materials," *Chemical engineering science*, vol. 61, no. 7, pp. 2230–2238, 2006.

[31] C. Liu and A. J. Bard, "Electrostatic electrochemistry at insulators," *Nature materials*, vol. 7, no. 6, pp. 505–509, 2008.

[32] S. Piperno, H. Cohen, T. Bendokov, M. Lahav, and I. Lubomirsky, "Comments on the concept of cryptoelectrons on dielectric surfaces," *Proc. ESA Annual Meeting on Electrostatics*, 2011.

[33] J. Lowell and W. S. Truscott, "Triboelectrification of identical insulators. II. Theory and further experiments," *Journal of Physics D: Applied Physics*, vol. 19, no. 7, p. 1281, 1986. [Online]. Available: http://stacks.iop.org/0022-3727/19/i=7/a=018

[34] D. J. Lacks and A. Levandovsky, "Effect of particle size distribution on the polarity of triboelectric charging in granular insulator systems," *Journal*

of Electrostatics, vol. 65, no. 2, pp. 107–112, 2007. [Online]. Available: http://www.sciencedirect.com/science/article/pii/S0304388606000866

[35] H. T. Baytekin, B. Baytekin, J. T. Incorvati, and B. A. Grzybowski, "Material transfer and polarity reversal in contact charging," *Angewandte Chemie International Edition*, vol. 51, no. 20, pp. 4843–4847, 2012. [Online]. Available: http://dx.doi.org/10.1002/anie.201200057

[36] T. A. L. Burgo, T. R. D. Ducati, K. R. Francisco, K. J. Clinckspoor, F. Galembeck, and S. E. Galembeck, "Triboelectricity: Macroscopic Charge Patterns Formed by Self-Arraying Ions on Polymer Surfaces," *Langmuir*, vol. 28, no. 19, pp. 7407–7416, 2012. [Online]. Available: http://dx.doi.org/10.1021/la301228j

[37] M. Sakaguchi, Y. Miwa, S. Hara, Y. Sugino, K. Yamamoto, and S. Shimada, "Triboelectricity in polymers: effects of the ionic nature of carbon–carbon bonds in the polymer main chain on charge due to yield of mechano-anions produced by heterogeneous scission of the carbon–carbon bond by mechanical fracture," *Journal of electrostatics*, vol. 62, no. 1, pp. 35–50, 2004.

[38] M. Sakaguchi, M. Makino, T. Ohura, and T. Iwata, "Contact electrification of polymers due to electron transfer among mechano anions, mechano cations and mechano radicals," *Journal of Electrostatics*, vol. 72, no. 5, pp. 412 – 416, 2014. [Online]. Available: http://www.sciencedirect.com/science/article/pii/S0304388614000515

[39] M. W. Williams, "What creates static electricity?" *American Scientist*, vol. 100, no. 4, pp. 316–323, 2012. [Online]. Available: https://search.proquest.com/docview/1029869187?accountid=27303

[40] A. F. Diaz, "Contact electrification of materials: The chemistry of ions on polymer surfaces," *The Journal of Adhesion*, vol. 67, no. 1-4, pp. 111–122, 1998. [Online]. Available: http://dx.doi.org/10.1080/00218469808011102

[41] R. Zangi and J. B. F. N. Engberts, "Physisorption of hydroxide ions from aqueous solution to a hydrophobic surface," *Journal of the American Chemical Society*, vol. 127, no. 7, pp. 2272–2276, 2005, pMID: 15713106. [Online]. Available: http://dx.doi.org/10.1021/ja044426f

[42] J. K. Beattie, "The intrinsic charge on hydrophobic microfluidic substrates," *Lab Chip*, vol. 6, pp. 1409–1411, 2006. [Online]. Available: http://dx.doi.org/10.1039/B610537H

[43] N. Knorr, "Squeezing out hydrated protons: low-frictional-energy triboelectric insulator charging on a microscopic scale," *AIP Advances*, vol. 1, no. 2, p. 022119, 2011. [Online]. Available: http://aip.scitation.org/doi/abs/10.1063/1.3592522

[44] D. B. Asay and S. H. Kim, "Evolution of the adsorbed water layer structure on silicon oxide at room temperature," *The Journal of Physical Chemistry B*, vol. 109, no. 35, pp. 16 760–16 763, 2005, pMID: 16853134. [Online]. Available: http://dx.doi.org/10.1021/jp053042o

[45] J. Lowell and A. C. Rose-Innes, "Contact electrification," *Advances in Physics*, vol. 29, no. 6, pp. 947–1023, 1980. [Online]. Available: http://dx.doi.org/10.1080/00018738000101466

[46] G. S. P. Castle, "Contact charging between insulators," *Journal of Electrostatics*, vol. 40, pp. 13–20, 1997. [Online]. Available: http://www.sciencedirect.com/science/article/pii/S0304388697000090

[47] L. Schein, M. LaHa, and D. Novotny, "Theory of insulator charging," *Physics Letters A*, vol. 167, no. 1, pp. 79–83, 1992.

[48] F. S. Ali, M. A. Ali, G. Castle, and I. Inculet, "Charge exchange model of a disperse system of spherical powder particles," in *Industry Applications Conference, 1998. Thirty-Third IAS Annual Meeting. The 1998 IEEE*, vol. 3. IEEE, 1998, pp. 1884–1891.

[49] J. Laurentie, P. Traoré, and L. Dascalescu, "Discrete element modeling of triboelectric charging of insulating materials in vibrated granular beds," *Journal of Electrostatics*, vol. 71, no. 6, pp. 951–957, 2013.

[50] J.-C. Laurentie, P. Traore, C. Dragan, and L. Dascalescu, "Numerical modeling of triboelectric charging of granular materials in vibrated beds," in *Industry Applications Society Annual Meeting (IAS), 2010 IEEE*. IEEE, 2010, pp. 1–6.

[51] M. Mizutani, M. Yasuda, and S. Matsusaka, "Advanced characterization of particles triboelectrically charged by a two-stage system with vibrations and external electric fields," *Advanced Powder Technology*, vol. 26, no. 2,

pp. 454–461, 2015. [Online]. Available: http://www.sciencedirect.com/science/article/pii/S0921883114003148

[52] W. P. I.S. Grant, *Electromagnetism (2nd ed.)*. Manchester Physics, John Wiley Sons., 2008.

[53] R. Feynman, R.P.; Leighton and M. Sands, *Feynman Lectures on Physics: Volume 2, Chapter 15: Application of Gauss's law, Chapter 10: Dielectrics*. Addison-Wesley, 1964.

[54] R. G. Rokkam, R. O. Fox, and M. E. Muhle, "Computational fluid dynamics and electrostatic modeling of polymerization fluidized-bed reactors," *Powder Technology*, vol. 203, no. 2, pp. 109–124, 2010. [Online]. Available: http://www.sciencedirect.com/science/article/pii/S0032591010001828

[55] W. Thielicke and E. Stamhuis, "Pivlab – towards user-friendly, affordable and accurate digital particle image velocimetry in matlab." *Journal of Open Research Software*, vol. 2, no. 1, 2014.

[56] L. Zhuravlev, "The surface chemistry of amorphous silica. zhuravlev model," *Colloids and Surfaces A: Physicochemical and Engineering Aspects*, vol. 173, no. 1, pp. 1–38, 2000.

[57] S. H. Behrens and D. G. Grier, "The charge of glass and silica surfaces," *The Journal of Chemical Physics*, vol. 115, no. 14, pp. 6716–6721, 2001.

[58] J. Kolehmainen, P. Sippola, O. Raitanen, A. Ozel, C. Boyce, P. Saarenrinne, and S. Sundaresan, "Modeling Effect of Humidity on Triboelectric Charging of Polyethylene Particles in a Vertically Vibrated Glass Container (Submitted)," 2017.

APPENDIX A. THE ELECTRIC FIELD ON THE WALLS

A motion picture similar to Figure 6.13 would reveal streams of negative particles travelling up and down along the strongly charged wall layer. However, it seems that these particles are not able to adhere to the positively charged wall particles. Figure 1 shows a possible reason for this: the long-range electric field strongly repels the negative particles from the wall. The magnitude of the repulsive electric field is ≈ 800 kV/m, while the magnitude of the attractive field due to the positive particles on the wall is ≈ 600 kV/m.

The notable step change in the long-range field seen in Figure 1 is due to the fact that the long-range field is applied cell-by-cell to each particle, without any interpolating. This is in line with Kolehmainen *et al.*, who argued that interpolating the electric field would distort the electric force experienced by each particle. In the case of insulating walls however, the surface charge on the wall causes a strong electric field, which then spreads over the cells next to the wall. This computational artefact seems to prevent the negatively charged particles entering the outermost cells of the bed at all.

Introducing an appropriate interpolation method, the long-range electric field on particles would shift smoothly from a strong field on the wall to a weaker field in the bed. Another option would be to introduce a thin boundary layer along the wall. Currently, no boundary layer is introduced in order to keep the cell size greater than the particle size also on the walls.

It is suspected that a robust interpolation method would yield weaker long-range field outside the first particle layer on the wall, allowing the negatively charged particles from the inner bed to attach on the positively charged wall layer. Unfortunately, the built-in interpolation methods of OpenFOAM seem to produce inconsistent results when interpolating the electric field to the particles.

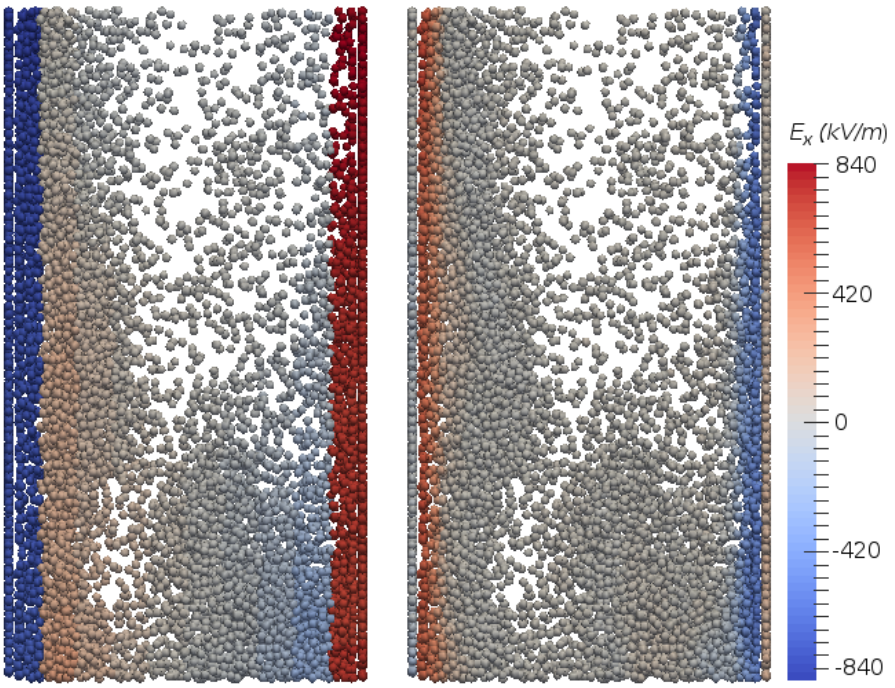

Figure 1 *The electric field strength in x-direction corresponding to Figure 6.13. Left hand side: Long-range field, right-hand side: short-range field. Same scale is used for both pictures.*

APPENDIX B. THE EFFECT OF THE ACCELERATION FACTOR

Correspondingly to the results of Kolehmainen *et al.* [19], increasing the acceleration factor does not affect significantly the total charge accumulated in the bed. However, the acceleration alters the particle charge distribution. The charge-to-mass ratios in the case of $\Delta\varphi/(z_c e) = 886$ kV/m obtained by using two different acceleration factors are given in Figure 2.

The charge distributions corresponding the cases shown in Figure 2 are shown in Figure 3. The charge distribution is clearly bimodal; corresponding to Figure 6.15, most of the particles are only slightly charged, appearing as a sharp peak near zero charge. The lower peak with a higher absolute charge accounts for the strongly charged particles on the wall. Increasing the acceleration factor shifts the peaks so that the wall particles hold even greater portion of the total charge.

This phenomenon can be explained through the screening effect of the layer of particles on the wall. As the acceleration factor increases, the particles in contact with wall rapidly achieve a sufficient amount of charge to be attracted to the wall. The faster the formation of the wall layer is, the less charge is spread to the bed interior. This is also illustrated in Figure 4, where the average charge in the wall layer and in the interior are plotted separately for both the cases.

Basing on Figure 4, the charge in the wall layer rises initially much faster in the more accelerated case, but after $at \approx 10$ s the difference between the two cases stays relatively constant. All in all, the acceleration factor has a positive correlation with the portion of the charge held by the particles on the wall. However, the saturation charges obtained in simulations are not greatly affected when used a reasonable acceleration factor.

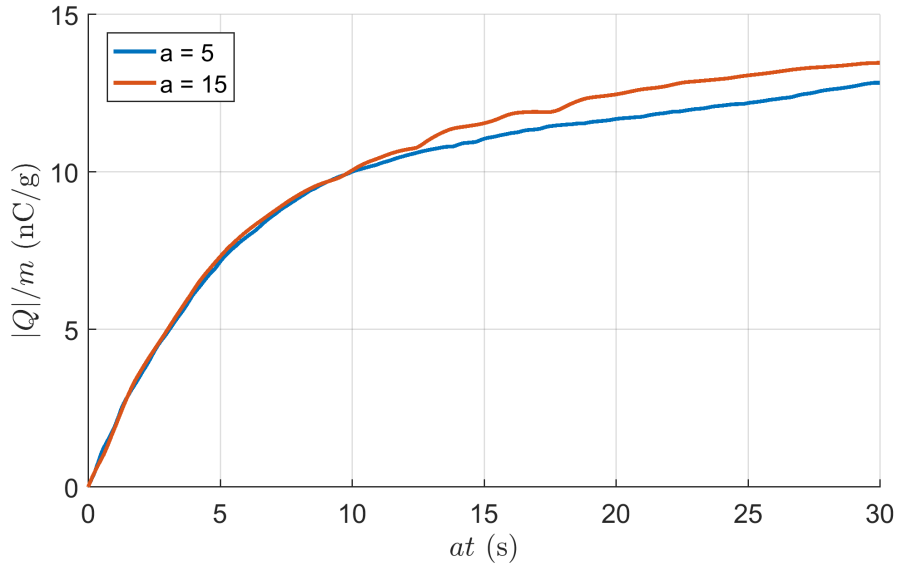

***Figure** 2 The time evolution of the charge-to-mass ratio in with using $\Delta\varphi/(z_c e) = 886$ kV/m and acceleration factors $a = 5$ and $a = 15$.*

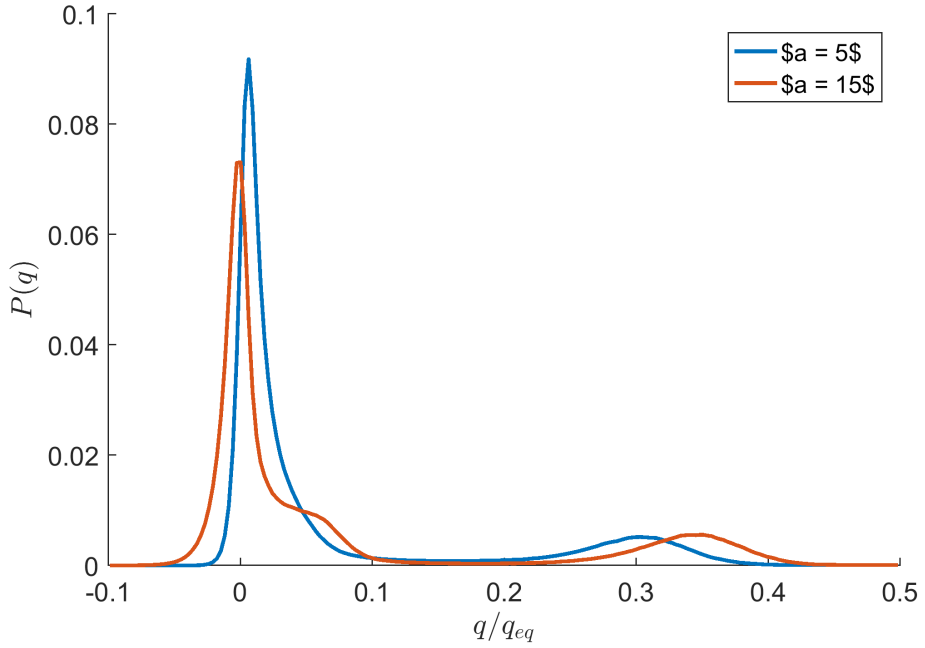

***Figure** 3 The probability density function for any particle having a charge q during the pseudo-steady state at = 20..30 s with using $\Delta\varphi/(z_c e) = 886$ kV/m and acceleration factors $a = 5$ and $a = 15$.*

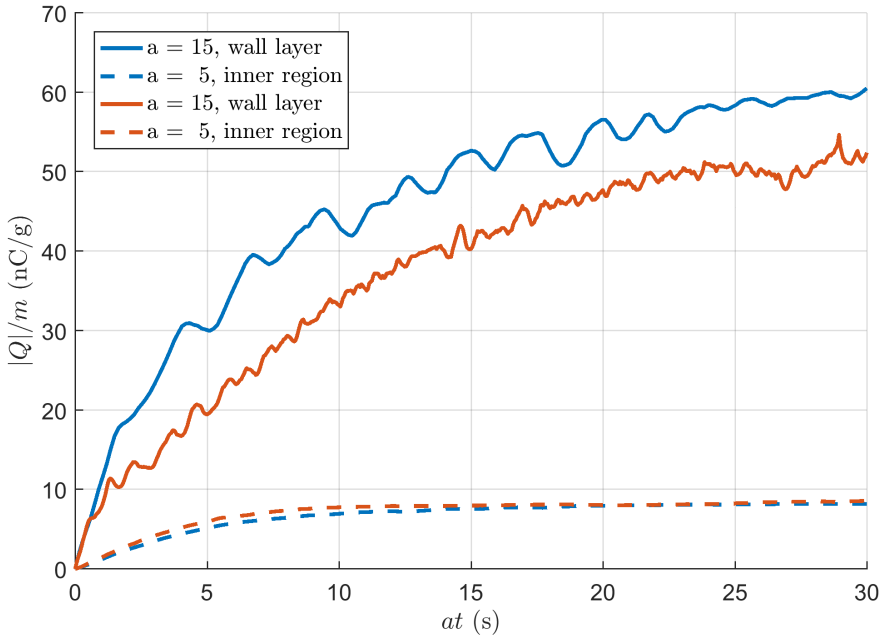

Figure 4 *The time evolution of the charge-to-mass ratio in the wall layer and the core of the bed in with using* $\Delta\varphi/(z_c e) = 886$ kV/m *and acceleration factors* $a = 5$ *and* $a = 15$.